A Two-Component Regulatory System Mediates Quorum Sensing–Dependent Morphology and Motility Transitions in the Archaeon *Haloferax volcanii*

Jacob A. Cote[1], Priyanka Chatterjee[1], Marco Garcia[2], Ran Tao[3], Arnold Mathijssen[3], and Mechthild Pohlschroder[1]*

[1]Perelman School of Medicine, University of Pennsylvania, Philadelphia, Pennsylvania 19104
[2]Department of Biology, University of Pennsylvania, Philadelphia, Pennsylvania 19104
[3]Department of Physics and Astronomy, University of Pennsylvania, Philadelphia, Pennsylvania 19104

Corresponding author: Mechthild Pohlschröder

Email: pohlschr@sas.upenn.edu

ABSTRACT

Quorum sensing (QS) enables microorganisms—including bacteria, eukaryotes, and viruses—to coordinate collective behaviors in response to population density. Despite their ecological and evolutionary significance, QS mechanisms in Archaea remain poorly characterized. The halophilic archaeon *Haloferax volcanii* provides a model for archaeal QS, transitioning from motile rods to non-motile disks in a density-dependent response to a secreted disk-forming signal (DFS). To identify components of the DFS regulatory network, we screened for spontaneous mutants that retained motility in DFS-containing soft-agar medium. One candidate, *HVO_1357*, encodes a predicted response regulator located adjacent to a histidine kinase (*HVO_1356*) and a second response regulator (*HVO_1358*), consistent with an extended two-component regulatory system (TCS). Based on our results, these genes encode quorum-sensing associated regulators (Qar), therefore, we propose rename them *qarA* (*HVO_1357*), *qarB* (*HVO_1356*), and *qarC* (*HVO_1358*). Deletion of *qarA* enabled cells to swim on DFS-containing soft-agar plates and conferred hypermotility on standard soft-agar media; however, these phenotypes were not due to changes in motility-related parameters, but a reduced sensitivity to DFS for induction of the non-motile, disk-shaped state. In contrast, Δ*qarB* and Δ*qarC* strains were non-motile and exhibited premature disk formation during normal growth. Suppressor mutations that restored motility to Δ*qarB* and Δ*qarC* mapped exclusively to *qarA*, suggesting QarA is the central regulator of this system. Transcriptomic analyses revealed that *qarA* deletion leads to upregulation of genes involved in motility and rod-shape formation. Together, these findings reveal *qarABC* as a DFS-responsive regulatory module and represent the first TCS in archaea shown to control QS-dependent behavior.

IMPORTANCE

Archaea are ubiquitous and play key roles across diverse ecosystems—including human microbiomes—yet little is known about how they communicate with one another and with other organisms, or how these interactions shape their ecological impact. Such intercellular communication, including quorum sensing (QS), allows microorganisms to coordinate behaviors critical for survival, adaptation, and community organization. In this study, we identify the first archaeal two-component regulatory system that is involved in QS-dependent regulation, providing a foundation for understanding how organisms in this domain sense and respond to population cues. By revealing a previously unknown aspect of archaeal biology, this work represents an important step toward understanding how archaeal communication shapes both their physiology and their interactions within complex microbial communities.

INTRODUCTION

Microorganisms rely on intercellular communication to coordinate behaviors that promote survival, competition, and adaptation in fluctuating environments. One of the best-characterized mechanisms of microbial communication is quorum sensing (QS), a process that enables density-dependent regulation of gene expression through the production and detection of secreted signaling molecules. When signal concentrations reach a threshold, cells alter transcriptional programs to coordinate behaviors like bioluminescence, biofilm formation, competence, motility, and sporulation (1-4). In gram-negative bacteria, QS often involves acyl-homoserine lactones (AHLs), exemplified by the LuxI/LuxR system in *Vibrio* species, where LuxI synthesizes AHLs that are bound by LuxR, which, once a threshold level is exceeded, activates QS-regulated genes (5). In contrast, gram-positive bacteria typically use secreted peptides as signals, and two-component regulatory systems (TCS) as signal transduction and response pathways (6). QS-like mechanisms have also been identified in fungi and viruses (7, 8), but in archaea quorum sensing remains largely unexplored, representing a major gap in our understanding of microbial communication.

Archaea possess unique physiologies and enzymes with considerable biotechnological potential (9, 10) and, due to their close evolutionary relationship to eukaryotes, serve as powerful models for studying fundamental cellular processes and the origins of eukaryotic biology (11-13). While archaea are recognized as ubiquitous members of environmental microbiomes that play critical roles in global biogeochemical cycles (14-17), they are also increasingly detected in human and animal microbiomes, where their ecological functions and impacts on host health remain poorly understood (18, 19). Despite these remarkable features, archaea remain deeply understudied compared to their bacterial and eukaryotic counterparts. Processes such as quorum sensing and other forms of intercellular signaling may provide mechanisms for communication within archaeal communities in microbiomes, as well as for interdomain communication with bacteria and eukaryotes (20). Understanding the molecular signals and regulatory pathways that mediate these interactions is therefore essential for revealing the broader ecological and physiological roles of archaea across diverse environments.

To date, QS-like behaviors have been reported in only a few archaea. These include *Natrialba magadii*, which exhibits growth phase–dependent Nep protease secretion (21); *Halorubrum lacusprofundi*, where culture supernatants enhance biofilm formation (22, 23); and *Methanosaeta harundinacea*, in which carboxy-AHLs are proposed to mediate density-dependent morphological changes (24). The authors of the latter study also identified a TCS that might be involved in the quorum sensing regulatory pathway, but in vivo data have not yet supported this, potentially due to the challenges to genetically manipulate this archaeon (25). In contrast, the model archaeon *Haloferax volcanii* combines a recently

118 identified quorum sensing–like behavior (20) with genetic tractability and facile growth
119 conditions, making it an ideal platform to study archaeal intercellular signaling (20, 26).
120 In *Hfx. volcanii*, cell morphology changes in a density-dependent manner: low-
121 density cultures are composed of motile, rod-shaped cells, whereas high-density cultures
122 consist of non-motile, pleomorphic disk-shaped cells (27-30). This transition can be
123 artificially induced at low cell densities by adding cell-free conditioned medium (CM) (20),
124 a hallmark of quorum sensing. Work done by Chatterjee *et al.* found that these cell shape
125 transitions are mediated by a secreted, yet-to-be-defined small molecule "disk-forming
126 signal" (DFS) (20). This study also identified two *Hfx. volcanii* proteins, DdfA and CirA, as
127 potential components of the DFS regulatory network (20). DdfA (disk-determining factor
128 A) is predicted to function as a shape-associated regulatory protein, as Δ*ddfA* cells remain
129 persistently rod-shaped (31). CirA, a KaiC-like signal transduction protein (32), shows a
130 similar phenotype, with Δ*cirA* cells also remaining rod-shaped (33). CirA has additionally
131 been linked to archaella gene regulation (33) and is more abundant in cells exposed to CM
132 (20). Proteomic data also identified a set of putative TCS proteins that may participate in
133 DFS sensing, analogous to the TCS-based quorum sensing systems seen in gram-positive
134 bacteria (20). One of these proteins is HVO_1356, a sensor histidine kinase encoded near
135 two response regulators: HVO_1357 and HVO_1358. Notably, mutations in *HVO_1357* were
136 previously identified in hypermotile isolates by Collins *et al.* (34), suggesting these proteins
137 may play a role in regulating motility-related responses to DFS.
138 TCS are among the most versatile and widespread signaling mechanisms in
139 prokaryotes, enabling cells to sense and respond to environmental and intercellular cues
140 through reversible phosphorylation cascades. Each system comprises a sensor histidine
141 kinase, which autophosphorylates at a conserved histidine residue, and a response
142 regulator that receives the phosphoryl group at a conserved aspartate in the receiver (REC)
143 domain to modulate its activity (35, 36). The histidine kinase detects various signals—
144 either directly or indirectly—and adjusts the phosphorylation state of the response
145 regulator by balancing its kinase and phosphatase activities (35-37). The response
146 regulator in turn orchestrates cellular functions depending on the type of output domain it
147 contains (37). In *E. coli*, as many as 30 TCS have been experimentally defined (38, 39). In
148 contrast, archaeal TCSs remain poorly understood, with only a few experimental studies
149 reported to date (25, 40, 41). Bioinformatic analyses, however, reveal striking differences
150 between bacterial and archaeal TCS components. In bacteria, sensor kinases are typically
151 membrane-bound, response regulators commonly possess DNA-binding domains, and
152 kinases and regulators generally occur in pairs (42). In archaea, by contrast, sensor kinases
153 are often cytosolic, response regulators frequently lack output domains, and kinases
154 commonly outnumber response regulators in the genome (42). These distinctions suggest
155 that archaeal TCSs may have evolved fundamentally different signaling architectures (42),
156 underscoring the need for further investigation into these systems.

157 In this study, we used phenotypic screens and reverse genetics approaches to
158 expand our understanding of the DFS regulatory network. Our results show that *HVO_1356*,
159 *HVO_1357*, and *HVO_1358* form a regulatory module that controls motility and cell-shape
160 responses to DFS. HVO_1357 functions as the central regulator, promoting rod-to-disk
161 shape transitions in response to DFS. In contrast, HVO_1356 and HVO_1358 are essential
162 for motility and appear to modulate the activity of HVO_1357. Together, these results
163 identify HVO_1356–HVO_1358 as quorum-sensing–associated regulators (Qar) that form a
164 DFS-responsive two-component system mediating quorum-sensing–dependent behaviors
165 in *Hfx. volcanii*—the first such system linked to quorum sensing and among the earliest
166 characterized in Archaea.
167
168 **RESULTS**
169 **Identification of mutants less responsive to DFS-dependent motility inhibition**
170 We previously showed that wild-type *Hfx. volcanii* cannot swim on soft-agar plates
171 containing conditioned media (CM), whereas knockout strains of *cirA* and *ddfA* can (20). In
172 an attempt to identify additional proteins involved in sensing or responding to the quorum-
173 sensing signal in CM, we adopted a screen which previously was used to identify
174 hypermotile mutants (34). Mid-log liquid cultures were inoculated as a line across soft-agar
175 plates containing 25% CM. Under these conditions, wild-type cells were non-motile;
176 however, spontaneous mutants with reduced response to DFS regained motility and moved
177 away from the inoculation line, forming flares (Fig. 1). Cells from the edge of such flares
178 were isolated and re-stabbed on CM-containing plates to confirm that they are able to
179 swim in the presence of DFS. Mutants isolated by this procedure were then subjected to
180 whole-genome sequencing. Two independent rounds of this screen yielded 23 isolates, and
181 sequencing identified mutations in 21 of these, including disruptions in *cirA* (five isolates)
182 and *ddfA* (one isolate), validating that our screen can identify genes of interest in the DFS
183 sensing and response pathway (Table 1; Table S1).
184 One mutant carried a large deletion spanning *HVO_2001–HVO_2069*, which includes
185 genes involved in cell-shape regulation such as *cetZ5*, *volA*, and components of the *agl15*-
186 dependent *N*-glycosylation pathway (Table 1, Table S1) (31). Additional mutations were
187 identified in *cdc48a* (*HVO_2380*, AAA-type ATPase; one isolate), *HVO_2649* (one isolate),
188 and *HVO_2248* (two isolates)—genes previously linked to hypermotile phenotypes by
189 Collins *et al.* (34)—as well as in *HVO_A0350* (two isolates), *pgsA1* (*HVO_1136*, CDP-alcohol
190 1-architidyltransferase; one isolate), and *gltP2* (*HVO_2885*, SDF family transporter; one
191 isolate) (Table 1). For two isolates, we were unable to identify any mutations despite their
192 ability to swim in the presence of CM, likely due to variant calling challenges associated
193 with polyploid genomes.
194 In addition to the mutations described above, a final set of mutants highlighted
195 *HVO_1357*, which appeared in four independent isolates (Table 1); notably, this gene was

196 one of two major loci previously reported by Collins *et al*. to cause hypermotility when
197 disrupted (34). *HVO_1357* is predicted to encode a DNA-binding response regulator and is
198 structurally similar to the Bat protein of *Halobacterium salinarum* (OE3101R), which
199 regulates expression of the bacteriorhodopsin apoprotein (34, 43-45). Unlike Bat, which
200 contains a non-functional REC domain (Fig. S1) and has yet to be associated with other TCS
201 components, *HVO_1357* appears to function as part of a TCS as it is adjacent to two
202 additional TCS-associated genes—a sensor histidine kinase (*HVO_1356*) and a standalone
203 REC-domain response regulator (*HVO_1358*) (Fig. 2). As demonstrated below, because all
204 three genes in this cluster are related to quorum sensing, we propose naming them
205 quorum-sensing associated regulators (Qar), designating HVO_1357—which has the
206 strongest impact—as *qarA*, the histidine kinase HVO_1356 as *qarB*, and the response
207 regulator HVO_1358 as *qarC*.
208 Multiple sequence alignments with experimentally characterized archaeal and
209 bacterial regulators show QarA contains all key features of a response regulator (37),
210 including a conserved phosphorylatable aspartate (D67) and other characteristic motifs of
211 functional REC domains (Fig. S1a). In addition to the REC domain (IPR001789), QarA
212 contains single copies of HalX (IPR013971), GAF (IPR029016), BAT (IPR031803), and
213 HTH_10 (IPR007050) domains, making it a complex multi-domain response regulator (Fig.
214 2)(34). HalX is haloarchaea-specific and often fused to REC domains (42), while GAF
215 domains typically sense stimuli–such as cyclic nucleotides, small molecules, and light–and
216 appear to be common features of archaeal TCS proteins (42, 46). The BAT domain, of
217 unknown function, is usually paired with GAF and HTH_10, a DNA-binding helix-turn-helix
218 specific to Bat-type regulators (42). When gene disruptions in *qarA* from this study and
219 from Collins *et al.* (34) are mapped to these domains, most of the disruptions occur in the
220 BAT domain followed by the GAF and HTH domains (Fig. 2). Interestingly, no mutations
221 were observed in the REC or HalX domains.

222 **QarA negatively regulates swimming and restricts motility in the presence of CM**

223 To confirm that disruption of QarA induces hypermotility and enables swimming
224 motility in the presence of CM, we constructed deletion strain Δ*qarA*. Consistent with the
225 motility phenotypes observed by Collins *et al.* (34) and in our CM motility screens, Δ*qarA*
226 exhibits hypermotility on soft-agar plates (Fig. 3a) and is motile on soft-agar plates
227 supplemented with CM (Fig. 3b). Complementation of the deletion strain with *qarA*
228 expressed from pTA963, the commonly used overexpression plasmid in *Hfx. volcanii*, could
229 not be evaluated as the plasmid itself induces hypermotility for unknown reasons (47, 48).
230 Interestingly, we found pTA963 also enabled wild-type cells to swim in the presence of CM,
231 consistent with its ability to induce hypermotility (Fig. S3a). However, at least partial
232 complementation of Δ*qarA in trans* was observed on CM-containing soft-agar plates, where
233 overexpression of *qarA* reduced motility (Fig. S3a). Furthermore, the observed
234 hypermotility of the ΔqarA strain was not attributable to growth differences; the deletion

strain was similar to the wild-type upon OD_{600} measurements and upon determination of viable cell counts (Fig. S2a,b).

To assess whether loss of *qarA* affects microscopic swimming behaviors that could thereby influence motility on soft-agar plates (49, 50), we used live-cell tracking microscopy to quantify various motility parameters in liquid culture (Movie S1). Consistent with previous studies, we found both wild-type and Δ*qarA* displayed two distinct swimming velocities around $2.2\mu m/s$ and $4.4\mu m/s$, corresponding to forward and reverse swimming modes respectively (Fig. 4d)(29). However, we could find no biologically meaningful differences between wild-type and Δ*qarA* cells when comparing other parameters such as average swimming speed ($2.197\mu m/s$ vs $1.975\mu m/s$) or motile fractions (48.5% vs 46%) (Fig. 4b,c,d). We also attempted to quantify the average time between directional reversals (e.g. "turns or tumbles") for both strains; although the standard deviation was high—likely due to background noise—the mean values were similar between wild-type and Δ*qarA* cells and consistent with previously reported values for wild-type *Hfx. volcanii* (Fig. S4) (29). These results suggest that the increased motility of the Δ*qarA* strain is not due to changes in the motility characteristics of any given cell while it is in the motile phase, but rather it may have a defect in regulating when to adopt the motile-rod versus non-motile-disk state.

Δ*qarA* raises the DFS threshold for motility arrest

We hypothesized that the hypermotility of Δ*qarA* in regular soft-agar medium and its ability to swim on CM-containing plates result from altered sensing of the DFS signal, such that mutant cells require higher DFS concentrations to slow or stop motility. This delay in sensing allows Δ*qarA* cells to remain motile longer, with the rod-to-disk transition occurring only later in growth or upon addition of higher DFS levels. To test this, we monitored cell shape at different growth stages and with exogenous CM. In early-log phase, both wild-type and Δ*qarA* cells were rod-shaped, though Δ*qarA* cells were noticeably longer (Fig. 5a, b). By mid-log, many wild-type cells had converted to disks, whereas Δ*qarA* cells remained largely rod-shaped (Fig. 5b). In stationary phase or with 1% (10μL/mL) CM, Δ*qarA* cultures fully transitioned to disks (Fig 5b, c, d), thus precluding a defect in shape transitions. This makes it likely that QarA may modulate DFS sensitivity. We quantified this by exposing cells to low CM concentrations (0.2–4 μL/mL) and measuring early-log disk formation. Wild-type cells responded even at 0.2–0.6 μL/mL CM, whereas Δ*qarA* required ~1 μL/mL CM to initiate disk formation, reaching wild-type levels by 2 μL/mL (Fig. 5e). The shifted response curve demonstrates that deletion of *qarA* raises the DFS threshold needed for shape conversion, explaining why mutants are hypermotile in standard medium and retain motility on CM-containing plates, yet show no change in single-cell swimming behavior.

QarB and QarC are required for motility and maintenance of the motile rod shape

275 Previous bioinformatic analyses revealed that *qarB*, *qarA*, and *qarC* are located in
276 the same genomic region but are not organized as an operon (34, 51, 52). *qarB* encodes a
277 putative cytosolic sensor histidine kinase with conserved PAS and GAF sensory domains
278 but no transmembrane regions, suggesting it functions as a cytosolic sensor or interacts
279 with other membrane-bound components for signal transduction through the cell
280 membrane. *qarC* encodes a standalone response regulator containing a conserved receiver
281 domain but lacks an output domain—an arrangement common in archaea but rare in
282 bacteria (42). Both *qarB* and *qarC* encode the essential phosphorylatable residues H347
283 and D58 respectively, as well as other residues important for histidine kinase and REC
284 domain functions (Fig. S1a,b)
285 To define their roles in motility and cell shape, deletion mutants were generated and
286 compared to wild type and the Δ*qarA* strain. While Δ*qarB* and Δ*qarC* showed slightly lower
287 OD_{600} values (Fig. S2a), the viable counts at comparable growth times remained similar.
288 However, motility phenotypes of these mutants were striking: both were completely non-
289 motile on soft agar with or without 25% CM (Fig. 3a,b). Complementation with plasmid-
290 borne *qarB* or *qarC* restored motility to wild-type or near wild-type levels (Fig. S3b),
291 confirming that both genes are essential for motility.
292 Microscopy imaging revealed that in early log phase, Δ*qarB* and Δ*qarC* cells were
293 rod-shaped, yet significantly shorter than wild type and transitioned to disk morphology
294 earlier in growth (Fig. 5a,b). Although still rod-shaped, live-cell microscopy showed that
295 these rods were non-motile under conditions where wild-type and Δ*qarA* strains were
296 motile (Fig. 4a,b). When grown in the presence of CM, Δ*qarB* and Δ*qarC* cultures were fully
297 disk-shaped (Fig. 5c,d). Together, these results show that *qarB* and *qarC* are both required
298 for motility and may promote the motile state in response to environmental cues such as
299 DFS concentration.
300
301 ***qarA* influences transcription of motility, cell-shape, and TCS genes**
302 To identify genes differentially transcribed in the absence of the putative DNA-
303 binding response regulator QarA, we compared RNA-seq profiles of wild-type and Δ*qarA*
304 *Hfx. volcanii* at early-log and late-log phases (full datasets in Tables S2–S5).
305 **Early-log phase:** In Δ*qarA*, 60 differentially expressed genes (DEGs) were identified
306 (Fig. 6a; Table S3). Thirteen DEGs were upregulated, including genes encoding archaella
307 components *arlA1* (*HVO_1210*) and *arlA2* (*HVO_1211*), motor complex components *arlH*
308 (*HVO_1216*) and *arlI* (*HVO_1217*), and the chemotaxis adaptor *cheF* (HVO_1219), all of
309 which are important for motility (33, 53). Genes encoding proteins involved in rod
310 formation, *rdfA* (*HVO_2174*) and *sph3* (*HVO_2175*), were also upregulated (31). *HVO_2649*,
311 identified in our 25% CM screen as well as the previous hypermotility screen (34), was
312 similarly upregulated. The most highly upregulated genes were *HVO_B0192* and
313 *HVO_B0193*, encoding a putative transmembrane protein and transcriptional regulator
314 with a domain of unknown function (DUF7521), respectively.

315 In contrast, 47 genes were downregulated in the Δ*qarA* mutant. A notable finding
316 was the decreased expression of *qarC*. Another gene in this region, *HVO_1359*, encoding a
317 CPxCG zinc-finger protein, was also downregulated. The most strongly downregulated gene
318 overall was *HVO_B0276*, encoding a predicted drug/metabolite transporter (DMT)
319 superfamily protein. Functional enrichment analysis of early-log DEGs revealed, next to
320 motility, an overrepresentation of genes involved in signal transduction (Fig. 6c).
321 **Late-log phase:** RNA-seq analysis identified 41 DEGs in the Δ*qarA* strain, including
322 3 upregulated and 38 downregulated genes (Fig. 6b; Table S5). A key observation in late-
323 log was the pronounced downregulation of *qarC* and *HVO_1359*, the latter of which was
324 more strongly down-regulated at increased significance compared to the early-log dataset.
325 *HVO_B0276*, the most strongly downregulated gene in early-log, is also highly
326 downregulated in late-log but drops in relative rank, highlighting the increasing
327 prominence of potential TCS and regulatory components in late-log DFS responses.
328 The remaining late-log-specific DEGs included upregulation of *HVO_2375* (encoding
329 PstS family transporter), *HVO_2063*, and *HVO_A0133*—encoding a predicted glycine zipper
330 protein with a TAT secretion signal previously reported as highly abundant in both CM-
331 grown and rod-shaped cells (20, 31). Other downregulated late-log-specific genes included
332 *HVO_A0350* (encoding TAT lipoprotein) and *HVO_A0351*. Notably, two mutants with
333 disruptions in *HVO_A0350* were identified in our CM screen (Table 1), supporting a
334 potential role for this region in DFS-dependent phenotypes. Interestingly, our
335 transcriptomics also identified several genes encoding surface-associated PQQ-like β-
336 propeller repeat proteins (*HVO_2606*, *HVO_2607*, *HVO_B0138*, *HVO_B0139*), highlighting
337 potential changes in adhesion, extracellular interactions, or signaling among late-log DEGs.
338 Like in the early-log dataset, functional enrichment analysis found enrichment of genes
339 with roles in signal transduction, but now also carbohydrate metabolism and transport,
340 likely due to surface-associated proteins like the PQQ-like β-propeller repeat proteins (Fig.
341 6d).
342 Several genes showed consistent changes across both early- and late-log datasets,
343 suggesting they contribute to a common regulatory program in response to loss of QarA.
344 These included *HVO_1310*, *HVO_0036 and HVO_2879* encoding a probable thioredoxin,
345 probable transmembrane protein, and ornithine cyclodeaminase, respectively. In addition,
346 multiple genes within or near the *HVO_2013–HVO_2020* locus, whose proteins were
347 previously implicated in cell shape determination, were differentially expressed (31).
348 Specifically, *HVO_2020* (encoding a membrane protein; DUF502 family) and *HVO_2024*
349 were downregulated in both datasets, whereas *HVO_2014* and *HVO_2017*, encoding a zinc
350 finger domain protein and a pentapeptide repeat protein, respectively, were identified only
351 in the early-log dataset.
352 To validate our RNA-seq results, real-time quantitative reverse transcriptase PCR
353 (qRT-PCR) was performed to compare transcript levels between the wild-type and Δ*qarA*
354 strains, focusing on representative genes identified as differentially expressed in the

355 transcriptomic analysis. Consistent with the RNA-seq data, *arlA1* was significantly
356 upregulated in Δ*qarA*, whereas *HVO_B0276* was downregulated (Fig. 7a). Expression of *rdfA*
357 also showed an overall increase in Δ*qarA* (mean relative expression = 1.32); however,
358 variability among biological replicates was high under the tested conditions, and the
359 difference was not statistically significant. Attempts to quantify *qarC* expression were
360 inconclusive due to apparent low transcript abundance (data not shown). Given that Δ*qarC*
361 displays opposite phenotypes to that of Δ*qarA*, and that deletion of *qarA* restores motility
362 in the Δ*qarC* background, we also examined the expression of these same genes in Δ*qarC* to
363 assess potential reciprocal regulation. As expected, *arlA1* and *rdfA* were downregulated in
364 Δ*qarC*, with *arlA1* showing little to no expression, consistent with its non-motile phenotype
365 (Fig. 7b). *HVO_B0276* exhibited a non-significant increase in expression (mean relative
366 expression = 1.4). Strikingly, *qarA* transcript levels were elevated approximately 4 times in
367 Δ*qarC* relative to the wild type. Transcriptomic observations that QarA promotes *qarC*
368 expression, and that *qarA* is overexpressed in cells lacking *qarB* are consistent with
369 spontaneous motile suppressors of Δ*qarB* and Δ*qarC* we occasionally observed emerging
370 from both non-motile strains (Fig S5). Whole-genome sequencing of three suppressors
371 from both deletion strain backgrounds revealed mutations in *qarA* (Table S1), suggesting
372 that QarA is functionally linked to QarB and QarC as its possible partners in this TCS
373 pathway.
374
375 **DISCUSSION**
376 In this study, we developed a genetic screen to identify components of the DFS-
377 mediated QS network in *Haloferax volcanii*. Through reverse genetics, microscopy, and
378 transcriptomic analyses, we uncovered a three-gene signaling module—*qarABC*—that
379 regulates cell shape and motility in response to DFS. Bioinformatic predictions indicate that
380 *qarA* encodes a multidomain DNA-binding response regulator, *qarB* a cytosolic histidine
381 kinase, and *qarC* a standalone REC-domain protein, all together forming a TCS-like
382 signaling architecture (Fig. 2, Fig. S1).
383 Functional analyses revealed that QarA acts as the principal effector of this pathway.
384 Deletion of *qarA* caused a pronounced hypermotile phenotype (Fig. 3a) that does not arise
385 from altered swimming behavior (Fig. 4) but rather from a shift in the DFS-dependent rod-
386 to-disk morphological transition (Fig. 5b). Δ*qarA* cells require substantially higher DFS
387 levels to convert to disk-shaped cells compared to wild-type cells, maintaining a larger
388 fraction of rod-shaped, motile cells (Fig. 5e). This reduced DFS sensitivity likely explains
389 the hypermotility observed on soft-agar plates: local DFS accumulation within the halo is
390 less effective at inducing the non-motile state, leaving a higher fraction of motile cells and
391 thereby increasing halo migration compared to wild type. Similarly, the DFS concentration
392 present in 25% CM soft agar plates is likely below the threshold needed to fully convert
393 Δ*qarA* cells to non-motile disks. Consistent with our view that QarA functions as a motility
394 repressor, plasmid-based overexpression of QarA not only reduced the ability of Δ*qarA* to

395 swim in the presence of DFS but also reduced motility below the plasmid-bearing wild-type
396 strain (Fig. S3a).
397 In contrast to the hypermotile Δ*qarA* strain, deletion of *qarB* or *qarC* resulted in
398 non-motile short rod-shaped cells (Fig. 3a; Fig. 4) that also transitioned prematurely to
399 disk-shaped cells (Fig. 5b). These reciprocal phenotypes, together with the observation that
400 motile suppressors of Δ*qarB* and Δ*qarC* carry secondary mutations in *qarA* (Table S1)
401 support a model in which QarB and QarC act upstream to inhibit QarA activity under low-
402 DFS conditions.
403 We propose that QarABC form a DFS-responsive signaling cascade that governs the
404 transition between motile and sessile states (Fig. 8). Based on their predicted domain
405 architectures, QarB and QarC likely function as a histidine kinase–response regulator pair,
406 forming the upstream module of a two-component–like system. Under low DFS conditions,
407 QarB and QarC maintain the motile, rod-shaped state by repressing QarA activity. As DFS
408 accumulates, QarB and QarC become inactivated, relieving repression of QarA. Activated
409 QarA then downregulates rod-associated genes such as *rdfA*, *sph3*, and *arlA1*—which are
410 upregulated in the Δ*qarA* mutant (Fig. 6a, 7a; Table S3)—thereby promoting conversion to
411 the non-motile, disk-shaped state.
412 Consistent with this model, the abundance of QarB decreases under high-DFS
413 conditions (20), suggesting that QarB becomes inactive as DFS levels rise, permitting
414 activation of QarA. Because QarC lacks a canonical output domain (Fig. 2), it is plausible
415 that it transmits this regulatory signal to QarA through direct protein–protein interactions
416 rather than through transcriptional control.
417 Interestingly, we also observed that *qarA* expression is elevated in Δ*qarC* cells (Fig.
418 7b), suggesting an additional regulatory link between QarC and QarA . This could reflect
419 indirect control via other transcriptional regulators of *qarA*, or possibly autoregulation by
420 QarA itself, a mechanism commonly observed among response regulators (36). If QarA
421 indeed activates its own expression, this feedback could amplify its activity once repression
422 by QarB/C is lost. Such a model would explain the reciprocal phenotypes between the
423 Δ*qarB*/Δ*qarC* strains and Δ*qarA*: in both cases, premature QarA activation—driven by loss
424 of upstream inhibition and potential positive feedback—would promote early transition to
425 the non-motile, disk-shaped state even under low DFS conditions. Notably, QarA also
426 promotes expression of *qarC* (Fig. 6a,b), forming a regulatory loop in which QarA activates
427 its own repressor—an arrangement that may serve to fine-tune or stabilize the transition
428 between motile and non-motile states.
429 Finally, although QarA contains a conserved REC domain suggestive of
430 phosphorylation, we detected no mutations within this region in our suppressor analyses.
431 Thus, the functional significance of QarA phosphorylation remains unresolved, but it may
432 represent an additional regulatory layer within the DFS-responsive QarABC signaling
433 cascade.

434 Transcriptomic profiling also revealed that QarA governs a broader regulatory
435 network linking DFS signaling to motility, morphology, and small-molecule transport.
436 Among the most strongly downregulated genes in Δ*qarA* was *HVO_B0276* (Fig. 6a,b; Table
437 S3,5), encoding a predicted DMT superfamily transporter previously identified as a
438 regulatory target of the metabolic regulator TbsP, which indirectly influences cell-shape
439 transitions in *Hfx. volcanii* (54). Given that the mechanism of DFS secretion remains
440 unknown, *HVO_B0276* represents a compelling candidate for mediating DFS trafficking.
441 Two additional genes, *HVO_B0192* and *HVO_B0193*, were strongly upregulated in the
442 *qarA* knockout during early-log phase (Fig. 6a). Both genes are repressed by the cell
443 division regulator CdsR, suggesting that loss of QarA disrupts early shape-related
444 transcriptional programs (55). This finding supports the idea that the QarABC system
445 functions early in growth to sense and respond to low levels of accumulating DFS. It is
446 likely that at higher cell density surrounding nutrients are limited and the disk shape
447 promotes better nutrient uptake. Thus, the QarABC system may allow cells to initiate the
448 rod-to-disk transition ensuring they are fully disk-shaped by later growth phases when
449 nutrients become limiting. Consistent with this model, Δ*qarB* and Δ*qarC* mutants form
450 short rods during early-log phase (Fig. 5a) but are non-motile (Fig. 3a; Fig. 4), suggesting
451 that the shape-transition program has already been triggered—suppressing motility before
452 morphological conversion to disks is complete.
453 Beyond these DFS pathway candidates, we also identified a consistent group of
454 differentially expressed genes across both early- and late-log datasets (Fig. 6a,b), including
455 *HVO_1310, HVO_0036,* and *HVO_2879,* encoding a probable thioredoxin, predicted
456 transmembrane protein,and ornithine cyclodeaminase, respectively, and the *HVO_2013–*
457 *HVO_2020* region, which encodes multiple shape-related factors in *Hfx. volcanii* (31).
458 Another intriguing candidate is *HVO_1359*, located immediately downstream of *qarABC* and
459 is co-transcribed with *qarC* and *HVO_1360* (Fig. 2) (51, 52). Although *HVO_1359* shows
460 modest differential regulation in early-log phase, it becomes one of the most strongly
461 downregulated genes in late-log phase, suggesting a link to DFS accumulation (Fig. 6a,b).
462 Consistent with this, *HVO_1359* abundance is elevated in cells grown in the presence of high
463 DFS concentrations (20). *HVO_1359* encodes a small CPxCG-type zinc finger protein, part of
464 a conserved but poorly understood family implicated in haloarchaeal stress and signaling
465 regulation (56-58). Notably, *HVO_1359* shares homology and genomic context with the Brz
466 protein of *Hbt. salinarum*, located adjacent to the Bat regulator, with which it is thought to
467 function as a co-regulator of bacterio-opsin transcription (59, 60). This connection suggests
468 that *HVO_1359* may also act as a co-regulator with QarA in DFS signaling. Moreover, zinc
469 finger proteins and AAA-type ATPases, such as *cdc48a* identified in our CM QS bypass
470 screen (Table 1), frequently co-occur with Bat-type proteins in haloarchaeal genomes (60,
471 61), further suggesting that *HVO_1359* and *cdc48a* may also be components of the DFS
472 regulatory network.

The overall findings described in this work define a DFS-responsive signaling module that integrates environmental and community-derived cues to coordinate collective behavior in *Hfx. volcanii*. The QarABC system represents the first experimentally characterized TCS in Archaea with demonstrated roles in QS, exhibiting parallels to both bacterial architectures and archaeal-specific innovations such as standalone REC-domain proteins.

Future studies dissecting the mechanisms of DFS sensing, QarA signaling, and DFS production will deepen understanding of archaeal QS-like systems and their possible conservation across lineages. While the QarABC system initiates early shape transitions, the ability of Δ*qarA* cells to form disks at high DFS levels indicates additional pathways act downstream. Together, these directions will illuminate how archaeal communities use small-molecule signaling to regulate collective behaviors, for which the foundations have been laid in the current study.

METHODS

Plasmids, primers, and strains. The plasmids, primers, and strains generated through molecular cloning are listed in Table S6. Summarized sequencing results of strains generated through motility screens can be found in Table S1.

Growth conditions. *Hfx. volcanii* strains were grown at 45 °C in liquid (orbital shaker, 250 rpm, 2.54-cm orbital) or on solid semi-defined Casamino Acids (Hv-Cab) agar (1.5% [wt/vol]) medium (27), supplemented with tryptophan and uracil (50 μg mL^{-1} each). Uracil was omitted for strains carrying pTA963-based plasmids. Solid plates were incubated in sealable bags to prevent drying. *Escherichia coli* strains were grown at 37 °C in NZCYM medium, either in liquid or solid agar (1.5% [wt/vol]) supplemented with ampicillin (100 μg mL^{-1}). Growth of liquid cultures was monitored via OD_{600} (Thermo Spectronic 20+).

Preparation of conditioned medium (CM) and CM-agar plates. CM and CM-agar plates were prepared as previously described (20). Briefly, a 1L culture of *Hfx. volcanii* was grown to OD_{600} 1.5 and cells pelleted by centrifugation (Beckman Coulter Avanti J-25I, JA-10 rotor, 8,000 x *g*, 30 min). The resulting supernatant (CM) was then filtered (Millipore Stericup, 0.22 μm PVDF membrane) and stored at −20°C. Soft agar motility plates contained 0.35% [wt/vol] agar of Hv-Cab medium supplemented with CM to a final concentration of 25%.

Conditioned media motility screens. Colonies of wild type *Hfx. volcanii* were inoculated into 5 mL liquid medium and grown at 45 °C with continuous shaking until mid-log phase (OD_{600} ~0.5). Isolates from the MG series (Table S1) were stab-inoculated halfway into the agar with a sterile toothpick, then dragged horizontally within the agar to form a groove.

512 For SB series isolates (Table S1) , 20 µL culture was spotted onto CM soft-agar plates and a
513 line streaked across the surface with a sterile toothpick. One or two lines were streaked per
514 plate, followed by incubation at 45 °C for 4–5 days in a plastic box with wet paper towels,
515 changed daily, to prevent drying. Cells from the edge of well-separated outgrowth flares
516 were sampled with sterile toothpicks and streaked on Hv-Cab plates to isolate individual
517 suppressor strains. Colonies were re-stabbed on 25% CM soft-agar plates to confirm the
518 CM-swimming phenotype. Plates were imaged with the lid removed and photographing
519 from above or using a document scanner.
520
521 **Whole-genome sequencing of deletion and suppressor strains.** Genomic DNA was
522 extracted using the GeneJET Genomic DNA Purification Kit (Thermo Scientific) and
523 quantified with a Qubit 3.0 Fluorometer and BR dsDNA kit (Invitrogen). Illumina whole-
524 genome sequencing and variant calling were performed by SeqCenter (Pittsburgh, PA,
525 USA). Libraries were prepared using the tagmentation-based Illumina DNA Prep kit with
526 custom IDT 10 bp unique dual indices and a target insert size of 280 bp. Sequencing was
527 performed on a NovaSeq X Plus, generating 2 × 150 bp paired-end reads. Demultiplexing,
528 quality control, and adapter trimming were performed with bcl-convert (Illumina) (MG4-
529 10 v3.9.3; MG15-33 v4.0.3; SB strains v4.1.5). Variant calling was carried out with BreSeq
530 (MG4-10 v0.36.1; MG15-33 v0.37.1; SB strains v0.38.1) (62) using *Hfx. volcanii* DS2
531 (GCF_000025685.1) as a reference. Predicted mutations were compared to the
532 Pohlschröder H53 lab strain (https://doi.org/10.5281/zenodo.17419175) background to
533 identify newly mutated genes. For suppressor strains with no predicted mutations, the
534 "Unassigned missing coverage," "Unassigned new junction," and marginal prediction files
535 were manually inspected, prioritizing DEGs identified in our RNA-seq experiments.
536 Manually predicted mutations were confirmed by mapping reads to *Hfx. volcanii* DS2
537 (GCF_000025685.1) using the Geneious mapper (Geneious Prime v.2025.2.2; structural
538 variants, short insertions/deletions of any size, medium/low sensitivity). Strains with no
539 identified mutations were further screened for large insertions using ISCompare v1.0.5
540 with default parameters, with none being detected (63).
541
542 **Plasmid preparation and transformation.** The pTA131 plasmid was used to generate
543 chromosomal deletions (64), and the pTA963 plasmid was used for complementation
544 experiments (65). To prevent restriction of methylated DNA by *Hfx. volcanii*, plasmids were
545 first transformed into *E. coli* NEB 5-alpha, then into homemade *E. coli* DAM$^-$ strain DL739,
546 before transformation into *Hfx. volcanii*. Plasmid preparations for both *E. coli* strains were
547 performed using the PureLink Quick Plasmid Miniprep Kit (Invitrogen). *Hfx. volcanii*
548 transformations were carried out using the polyethylene glycol method (66), and *E. coli*
549 transformations by heat shock (67).
550

551 **Generation of chromosomal deletions in *Hfx. volcanii*.** Chromosomal deletions were
552 generated using the pop-in/pop-out method following transformation with pTA131-based
553 plasmids, as previously described (64). Constructs for deletion (pJC1, pJC2, pJC3) were
554 generated by amplifying ~750 nt flanking each gene via PCR, followed by overlap PCR
555 (primer sets 3–4, 7–8, 11–12). The fused upstream and downstream fragments were
556 cloned into pTA131 at XbaI and XhoI sites. Following transformation and selection,
557 deletions were confirmed by colony PCR using primers flanking and internal to the deleted
558 gene (primer sets 5–6, 9–10, 13–14). Deletion strains were further validated by whole-
559 genome sequencing and variant calling to confirm complete gene deletion and assess
560 secondary genome alterations.
561
562 **Construction of complementation plasmids.** The *HVO_1356*-StrepII expression plasmid
563 pJC4 was generated by PCR amplification of *HVO_1356* from *Hfx. volcanii* genomic DNA
564 using primer set 15 and cloning into pTA963. The corresponding complementation
565 plasmid, *HVO_1356*-StrepII-Myc (pJC6), was created by adding a Myc tag to pJC4 via site-
566 directed mutagenesis (New England BioLabs Q5 kit) with primer set 16. Similarly,
567 *HVO_1357*-StrepII (pJC5) was amplified with primer set 17 and cloned into pTA963, and
568 the complementation plasmid *HVO_1357*-StrepII-FLAG (pJC7) was obtained by introducing
569 a FLAG tag to pJC5 using site-directed mutagenesis with primer set 18. HA-StrepII-
570 *HVO_1358* (pJC8) was synthesized by Twist Bioscience (San Francisco, CA, USA).
571
572 **Growth curves.** Colonies of each strain were inoculated into 5 mL liquid medium and
573 grown at 45 °C with continuous shaking until mid-log phase (OD_{600} 0.3–0.5). Cultures were
574 diluted to OD_{600} 0.01 in 200 µL fresh medium per well of a non-treated, flat-bottom 96-well
575 plate (Corning). Growth was measured using a BioTek Epoch 2 microplate reader with
576 Gen6 software (Agilent v1.04). Four biological replicates were used per strain. To minimize
577 evaporation, empty wells were filled with 200 µL water, and a 2 °C gradient was applied to
578 the 45 °C incubator setting. Readings were taken every 30 min at 600 nm, with continuous
579 double-orbital shaking (335 rpm, 4 mm) between measurements, for a total of 72 h.
580
581 **Determination of viable cell counts.** Cultures for each strain were grown to mid-log
582 phase (OD_{600} 0.3–0.5). Cultures were diluted to OD_{600} 0.3 and serially ten-fold diluted. 30µL
583 of 10^{-3} to 10^{-5} dilutions were spread onto Hv-Cab solid agar plates and incubated for 3-5
584 days. Colonies were manually counted and reported as $\log_{10}$ CFU/mL of the original
585 culture.
586
587 **Motility assays and motility halo quantification.** Motility was assessed on 0.35%
588 [wt/vol] agar Hv-Cab medium. Colonies were inoculated into 5 mL liquid medium and
589 grown at 45 °C with continuous shaking until mid-log phase (OD_{600} 0.3–0.5). Cultures were
590 diluted to the lowest OD_{600} among the strains tested and stab-inoculated into the agar with

591 a toothpick. Plates were incubated upright at 45 °C in a plastic box with wet paper towels,
592 changed daily, to maintain humidity. After two days, plates were removed and imaged
593 following at least one day at room temperature to allow halos to darken. Images were
594 acquired using a document scanner, with lids removed. Halo areas were quantified as
595 previously described (54) using FIJI (68): the scale was calibrated to plate diameter, halos
596 were segmented with the threshold tool, and areas measured using the Analyze Particles
597 function.
598
599 **Cell shape microscopy.** *Hfx. volcanii* strains were inoculated from single colonies into
600 5 mL Hv-Cab liquid medium; for CM experiments, 50 µL CM (1% [vol/vol]) was added.
601 Cultures were grown to early-log (OD_{600} 0.045–0.050), mid-log (OD_{600} 0.30), or stationary
602 phase (72 h, OD_{600} ~1.9–3.0). For early- and mid-log cultures, 1 mL aliquots were
603 centrifuged at 4,900 × g for 6 min and pellets resuspended in their supernatant (~5 µL for
604 early-log, ~50 µL for mid-log). For imaging, 1.5 µL of resuspended pellet or stationary
605 culture was placed on glass slides (Fisher Scientific) and covered with No. 1 18 × 18 mm
606 coverslips (Globe Scientific Inc.), gently pressed to maintain a single cell layer. Images were
607 acquired on a Leica DMi8 inverted microscope with DFC9000 GT camera using Leica
608 Application Suite X (v3.6.0.20104). DIC and brightfield images were captured with a 100×
609 Plan Apochromat objective (NA 1.4, WD 0.09 mm). Brightfield images for quantification
610 were background-subtracted in FIJI (ImageJ v2.16.0/1.54p)(68) and analyzed in
611 CellProfiler (v4.2.8)(69). The FIJI macro and CellProfiler pipeline used are available at
612 https://doi.org/10.5281/zenodo.17419175.
613
614 **CM titration microscopy.** *Hfx. volcanii* strains were inoculated from single colonies into
615 5 mL Hv-Cab liquid medium containing 0.2, 0.6, 1, 2, or 4µL/mL CM. Cultures were grown
616 to early-log phase (OD_{600} 0.045–0.050) and imaged and analyzed using FIJI (ImageJ
617 v2.16.0/1.54p)(68) and CellProfiler (v4.2.8)(69) as described above. Fraction of disk-
618 shaped cells was calculated by finding the ratio of cells with the CellProfiler eccentricity
619 values below 0.9.
620
621 **Motility chamber construction.** Motility chambers were assembled using 24 × 50 mm
622 (Fisher Scientific) and 18 × 18 mm (Corning) No. 1 coverslips. Coverslips were cleaned in a
623 saturated KOH/ethanol bath for 30 min, rinsed with deionized water, and immersed in 1%
624 solution of polyvinylpyrrolidone K30 containing 0.01% Tween-20 for 1 h. Coverslips were
625 removed slowly, air-dried vertically, and baked at 120 °C for 1 h. Chambers were
626 constructed by placing two double layers of parafilm (~5 × 25 mm) ~8 mm apart on a large
627 prepared coverslip on a 95 °C hotplate, followed by covering them with a small prepared
628 coverslip to form an ~8 × 18 mm chamber with a height of ~200 µm.
629

630 **Live-cell tracking and analysis.** Cultures were grown to early-log phase (OD_{600} 0.045–
631 0.050) and diluted 1:5 (wild type, Δ*qarA*) or 1:2 (Δ*qarB*, Δ*qarC*) in pre-heated (45°C)
632 motility buffer (Hv-Cab medium with 1% [wt/vol] BSA). Motility chambers were partially
633 filled (~2/3) from one end with pre-heated motility buffer to further passivate glass
634 surfaces, then fully filled with diluted cells. Chamber ends were sealed with liquid VALAP
635 wax and imaged immediately. Swimming behavior was recorded on a Nikon TI2-E
636 microscope with a 20× CFI60 Plan Apochromat Lambda objective (NA 0.75, WD 1.0 mm)
637 under brightfield illumination. Videos were captured at 5 fps for 5 min using a Hamamatsu
638 Orca-Fusion Gen-III sCMOS camera using NIS-Elements (6.10.01). Cells were tracked near
639 the bottom coverslip. Videos were processed in FIJI, and trajectories were automatically
640 analyzed using a custom macro with TrackMate plugins (70, 71). For determination of non-
641 motile vs motile cells, $1\mu m/s$ was used as a threshold based on observations of non-motile
642 objects in our motility chambers.
643
644 **RNA extraction and purification.** Liquid cultures (5 mL) of each strain were grown at
645 45 °C with shaking to OD_{600} 0.05 (early-log) or 0.9 (late-log). Early-log (4–5 mL) and late-
646 log (0.5 mL) cultures were harvested and pelleted at 4,900 × g for 6 min. RNA was extracted
647 using the Qiagen RNeasy Plus Micro Kit, with lysates homogenized via QIAshredder
648 columns. For late-log RNA-seq and qRT-PCR samples, DNase digestion was performed
649 using the RNase-free DNase kit (Qiagen) followed by RNeasy MinElute Cleanup (Qiagen).
650 RNA concentration was measured with Qubit RNA Broad Range Assay Kits (Invitrogen),
651 and integrity assessed using RNA ScreenTape on a 4200 Tapestation (Agilent). All RNA-seq
652 and qRT-PCR samples had RINe values above 8.9 and 7.0, respectively.
653
654 **RNA sequencing and data analysis.** Cell pellets were collected and RNA extracted as
655 described previously. For early-log and late-log samples, four and three biological
656 replicates were collected, respectively. Purified RNA was sent to SeqCenter LLC
657 (Pittsburgh, PA, USA) for library preparation and sequencing. RNA was DNase-treated
658 (Invitrogen, RNase-free) prior to library preparation using Illumina Stranded Total RNA
659 Prep Ligation with Ribo-Zero Plus kit and 10 bp unique dual indices. Additional rRNA
660 depletion was performed with *Hfx. volcanii*-specific probes from Rados *et al*. (72).
661 Sequencing was performed on a NovaSeq X Plus with 2 × 150 bp paired-end reads.
662 Demultiplexing, quality control, and adapter trimming were done with bcl-convert (v4.2.4).
663 Paired-end RNA-seq reads were quality-checked, rRNA/tRNA reads were removed, and the
664 remaining reads were aligned to the *Hfx. volcanii* DS2 reference genome
665 (GCF_000025685.1) using minimap2 (73), with alignments processed using samtools (74).
666 Gene-level counts were obtained with featureCounts from the Rsubread R package (75).
667 Differential expression between Δ*qarA* and wild type was analyzed using DESeq2 (76);
668 genes with <10 total counts were excluded. Log_2 fold changes were estimated with the
669 Wald test and shrinkage-adjusted using apeglm (77). Gene annotations, including product

670 descriptions, arCOG assignments, and COG functional classes, were obtained from RefSeq
671 and locus tag reference tables. Genes with adjusted p-values (Benjamini–Hochberg) <0.01
672 and $|\log_2 FC| > 0.58$ were considered differentially expressed. PCA and volcano plots were
673 generated with ggplot2 and plotly to visualize sample clustering and differential
674 expression. Functional enrichment of significant DEGs was assessed by comparing the
675 distribution of gene function categories in each DEG set to the genome-wide background
676 using Fisher's exact tests. The pipeline used to perform RNA-seq analyses can be found at
677 https://doi.org/10.5281/zenodo.17419175
678
679 **qPCR analysis.** Three biological replicates of Δ*qarA* and Δ*qarC* were collected as
680 previously described for early-log RNA samples, along with two sets of three biological
681 replicates of wild-type controls per comparison. cDNA was synthesized from 1 µg RNA
682 using the ProtoScript II First Strand cDNA Synthesis Kit (New England BioLabs) with
683 random primers; parallel negative controls without reverse transcriptase (-RT) were
684 prepared.
685 Primers for *Hfx. volcanii* genes *eif1a, arlA1, rdfA, HVO_1357, HVO_1358,* and
686 *HVO_B0276* were designed using Primer3 and synthesized as RxnReady™ primers. qRT-
687 PCR reactions (20 µL) contained 2× iTaq Universal SYBR Green Supermix (Bio-Rad), 5%
688 DMSO, 300 nM primers, and 8 µL of 1:125 diluted cDNA. No-template (NTC) and -RT
689 controls were included; reactions were considered acceptable if ΔCt ≤10 between sample
690 and control. Primer efficiencies determined via standard curves ranged from 85.5–99.5%.
691 Each reaction included three biological replicates, each with three technical replicates, run
692 on a QuantStudio 3 Real-Time PCR System (Applied Biosystems).
693 Thermal cycling conditions were: 94 °C for 2 min, then 40 cycles of 95 °C for 15 s
694 and 60 °C for 30 s (*eif1a*, *HVO_1357*, *HVO_B0276*) or 58 °C for 30 s (*arlA1*, *rdfA, HVO_1358)*.
695 SYBR Green fluorescence was recorded at each cycle's end, and the default melt curve
696 program following the qPCR run verified primer specificity. Relative expression was
697 calculated in Excel using the Pfaffl method (78), normalizing to *eif1a*, and compared to
698 wild-type controls to determine differential expression.
699
700 **DATA AVAILABILITY**
701 The raw RNA-seq data generated in this study have been deposited in the NCBI Sequence
702 Read Archive (SRA) under BioProject accession number PRJNA1347779. Additional
703 materials are available at https://doi.org/10.5281/zenodo.17419175, including: whole-
704 genome sequencing and variant-calling data for mutant, knockout, and background strains;
705 images, scripts, and processed data for cell-shape analyses; images and data for soft-agar
706 motility assays; live-cell tracking data; pipelines and key outputs from RNA-seq analyses;
707 and raw and processed qPCR data.
708

ACKNOWLEDGEMENTS

We acknowledge Kiara Escudero, Shalaya Brown, and Sophia Sun for their contributions to phenotypic assays and CM screens, respectively. We also thank Dr. Alexandre Bisson for his guidance with RNA-seq analysis and for providing rDNA-depletion probes. We gratefully acknowledge Dr. Friedhelm Pfeiffer, Dr. Fevzi Daldal, Dr. Yirui Hong, and Everlyne Mutua for their insightful feedback on the manuscript. This work was supported by the National Science Foundation (UPenn NSF-MBC2222076) and the University of Pennsylvania Research Fund. J.C. was supported by the National Science Foundation Graduate Research Fellowship. P.C. was supported by a National Institutes of Health Training Grant (UPenn T32 GM007229) as well as a National Institutes of Health Ruth L. Kirschstein National Research Service Award (1F31AI181536-01). M.G. was supported by a Merck/PennFERBS fellowship. A.M. acknowledges funding from the Charles E. Kaufman Foundation (Early Investigator Research Award KA2022-129523; New Initiative Research Award KA2024-144001) and the National Science Foundation (UPenn MRSEC DMR-2309043).

REFERENCES

1. Miller MB, Bassler BL. 2001. Quorum Sensing in Bacteria. Annual Review of Microbiology 55:165–199.
2. Bassler BL, Losick R. 2006. Bacterially Speaking. Cell 125:237–246.
3. Reading NC, Sperandio V. 2006. Quorum sensing: the many languages of bacteria. FEMS Microbiology Letters 254:1–11.
4. West SA, Winzer K, Gardner A, Diggle SP. 2012. Quorum sensing and the confusion about diffusion. Trends in Microbiology 20:586–594.
5. Soto-Aceves MP, Diggle SP, Greenberg EP. 2023. Microbial Primer: LuxR-LuxI Quorum Sensing. Microbiology 169.
6. Giannakara M, Koumandou VL. 2022. Evolution of two-component quorum sensing systems. Access Microbiology 4.
7. Hornby JM, Jensen EC, Lisec AD, Tasto JJ, Jahnke B, Shoemaker R, Dussault P, Nickerson KW. 2001. Quorum Sensing in the Dimorphic FungusCandida albicans Is Mediated by Farnesol. Applied and Environmental Microbiology 67:2982–2992.
8. Erez Z, Steinberger-Levy I, Shamir M, Doron S, Stokar-Avihail A, Peleg Y, Melamed S, Leavitt A, Savidor A, Albeck S, Amitai G, Sorek R. 2017. Communication between viruses guides lysis–lysogeny decisions. Nature 541:488–493.
9. Pfeifer K, Ergal İ, Koller M, Basen M, Schuster B, Rittmann SKMR. 2021. Archaea Biotechnology. Biotechnology Advances 47:107668.
10. Aparici-Carratalá D, Esclapez J, Bautista V, Bonete M-J, Camacho M. 2023. Archaea: current and potential biotechnological applications. Research in Microbiology 174:104080.
11. Eme L, Spang A, Lombard J, Stairs CW, Ettema TJG. 2017. Archaea and the origin of eukaryotes. Nature Reviews Microbiology 15:711–723.

12. López-García P, Moreira D. 2020. The Syntrophy hypothesis for the origin of eukaryotes revisited. Nature Microbiology 5:655–667.
13. Eme L, Tamarit D, Caceres EF, Stairs CW, De Anda V, Schön ME, Seitz KW, Dombrowski N, Lewis WH, Homa F, Saw JH, Lombard J, Nunoura T, Li W-J, Hua Z-S, Chen L-X, Banfield JF, John ES, Reysenbach A-L, Stott MB, Schramm A, Kjeldsen KU, Teske AP, Baker BJ, Ettema TJG. 2023. Inference and reconstruction of the heimdallarchaeial ancestry of eukaryotes. Nature 618:992–999.
14. Chaban B, Ng SYM, Jarrell KF. 2006. Archaeal habitats — from the extreme to the ordinary. Canadian Journal of Microbiology 52:73–116.
15. Offre P, Spang A, Schleper C. 2013. Archaea in Biogeochemical Cycles. Annual Review of Microbiology 67:437–457.
16. Baker BJ, De Anda V, Seitz KW, Dombrowski N, Santoro AE, Lloyd KG. 2020. Diversity, ecology and evolution of Archaea. Nature Microbiology 5:887–900.
17. Kim J-G, Gazi KS, Awala SI, Jung M-Y, Rhee S-K. 2021. Ammonia-oxidizing archaea in biological interactions. Journal of Microbiology 59:298–310.
18. Bang C, Schmitz RA. 2015. Archaea associated with human surfaces: not to be underestimated. FEMS Microbiology Reviews 39:631–648.
19. Moissl-Eichinger C, Pausan M, Taffner J, Berg G, Bang C, Schmitz RA. 2018. Archaea Are Interactive Components of Complex Microbiomes. Trends in Microbiology 26:70–85.
20. Chatterjee P, Consoli CE, Schiller H, Winter KK, McCallum ME, Schulze S, Pohlschroder M. 2025. Quorum sensing mediates morphology and motility transitions in the model archaeon Haloferax volcanii. mBio 16:e0090625.
21. Paggi RA, Madrid EA, D'Alessandro CP, Cerletti M, De Castro RE. 2010. Growth phase-dependent biosynthesis of Nep, a halolysin-like protease secreted by the alkaliphilic haloarchaeon Natrialba magadii. Letters in Applied Microbiology 51:36–41.
22. Charlesworth J, Kimyon O, Manefield M, Beloe CJ, Burns BP. 2020. Archaea join the conversation: detection of AHL-like activity across a range of archaeal isolates. FEMS Microbiology Letters 367.
23. Liao Y, Williams TJ, Ye J, Charlesworth J, Burns BP, Poljak A, Raftery MJ, Cavicchioli R. 2016. Morphological and proteomic analysis of biofilms from the Antarctic archaeon, Halorubrum lacusprofundi. Scientific Reports 6:37454.
24. Zhang G, Zhang F, Ding G, Li J, Guo X, Zhu J, Zhou L, Cai S, Liu X, Luo Y, Zhang G, Shi W, Dong X. 2012. Acyl homoserine lactone-based quorum sensing in a methanogenic archaeon. The ISME Journal 6:1336–1344.
25. Li J, Zheng X, Guo X, Qi L, Dong X. 2014. Characterization of an archaeal two-component system that regulates methanogenesis in Methanosaeta harundinacea. PLoS One 9:e95502.
26. Pohlschroder M, Schulze S, Pfeiffer F, Hong Y. 2025. Haloferax volcanii: a versatile model for studying archaeal biology. Journal of Bacteriology 207:e00062–25.

27. de Silva RT, Abdul-Halim MF, Pittrich DA, Brown HJ, Pohlschroder M, Duggin IG. 2021. Improved growth and morphological plasticity of Haloferax volcanii. Microbiology 167.
28. Nußbaum P, Ithurbide S, Walsh JC, Patro M, Delpech F, Rodriguez-Franco M, Curmi PMG, Duggin IG, Quax TEF, Albers S-V. 2020. An Oscillating MinD Protein Determines the Cellular Positioning of the Motility Machinery in Archaea. Current Biology 30:4956–4972.e4.
29. Li Z, Kinosita Y, Rodriguez-Franco M, Nußbaum P, Braun F, Delpech F, Quax TEF, Albers S-V. 2019. Positioning of the Motility Machinery in Halophilic Archaea. mBio 10:10.1128/mbio.00377–19.
30. Duggin IG, Aylett CH, Walsh JC, Michie KA, Wang Q, Turnbull L, Dawson EM, Harry EJ, Whitchurch CB, Amos LA, Löwe J. 2015. CetZ tubulin-like proteins control archaeal cell shape. Nature 519:362–5.
31. Schiller H, Hong Y, Kouassi J, Rados T, Kwak J, DiLucido A, Safer D, Marchfelder A, Pfeiffer F, Bisson A, Schulze S, Pohlschroder M. 2024. Identification of structural and regulatory cell-shape determinants in Haloferax volcanii. Nature Communications 15:1414.
32. Makarova KS, Galperin MY, Koonin EV. 2017. Proposed Role for KaiC-Like ATPases as Major Signal Transduction Hubs in Archaea. mBio 8:10.1128/mbio.01959–17.
33. Chatterjee P, Garcia MA, Cote JA, Yun K, Legerme GP, Habib R, Tripepi M, Young C, Kulp D, Dyall-Smith M, Pohlschroder M. 2024. Involvement of ArlI, ArlJ, and CirA in archaeal type IV pilin-mediated motility regulation. Journal of Bacteriology 206:e00089–24.
34. Collins M, Afolayan S, Igiraneza AB, Schiller H, Krespan E, Beiting DP, Dyall-Smith M, Pfeiffer F, Pohlschroder M. 2021. Mutations Affecting HVO_1357 or HVO_2248 Cause Hypermotility in Haloferax volcanii, Suggesting Roles in Motility Regulation. Genes 12:58.
35. Stock AM, Robinson VL, Goudreau PN. 2000. Two-Component Signal Transduction. Annual Review of Biochemistry 69:183–215.
36. Groisman EA. 2016. Feedback Control of Two-Component Regulatory Systems. Annu Rev Microbiol 70:103–24.
37. Gao R, Bouillet S, Stock AM. 2019. Structural Basis of Response Regulator Function. Annu Rev Microbiol 73:175–197.
38. Yamamoto K, Hirao K, Oshima T, Aiba H, Utsumi R, Ishihama A. 2005. Functional Characterization in Vitro of All Two-component Signal Transduction Systems from Escherichia coli*. Journal of Biological Chemistry 280:1448–1456.
39. Mizuno T. 1997. Compilation of All Genes Encoding Two-component Phosphotransfer Signal Transducers in the Genome of Escherichia coli. DNA Research 4:161–168.
40. Najnin T, Siddiqui KS, Taha, Elkaid N, Kornfeld G, Curmi PMG, Cavicchioli R. 2016. Characterization of a temperature-responsive two component regulatory system from the Antarctic archaeon, Methanococcoides burtonii. Scientific Reports 6:24278.

41. Rudolph J, Tolliday N, Schmitt C, Schuster SC, Oesterhelt D. 1995. Phosphorylation in halobacterial signal transduction. The EMBO Journal 14:4249–4257.
42. Galperin Michael Y, Makarova Kira S, Wolf Yuri I, Koonin Eugene V. 2018. Phyletic Distribution and Lineage-Specific Domain Architectures of Archaeal Two-Component Signal Transduction Systems. Journal of Bacteriology 200:10.1128/jb.00681–17.
43. Baliga NS, Kennedy SP, Ng WV, Hood L, DasSarma S. 2001. Genomic and genetic dissection of an archaeal regulon. Proceedings of the National Academy of Sciences 98:2521–2525.
44. Gropp F, Betlach MC. 1994. The bat gene of Halobacterium halobium encodes a trans-acting oxygen inducibility factor. Proceedings of the National Academy of Sciences 91:5475–5479.
45. Leong D, Boyer H, Betlach M. 1988. Transcription of genes involved in bacterio-opsin gene expression in mutants of a halophilic archaebacterium. Journal of Bacteriology 170:4910–4915.
46. Heikaus CC, Pandit J, Klevit RE. 2009. Cyclic Nucleotide Binding GAF Domains from Phosphodiesterases: Structural and Mechanistic Insights. Structure 17:1551–1557.
47. Abdul Halim MF, Karch KR, Zhou Y, Haft DH, Garcia BA, Pohlschroder M. 2015. Permuting the PGF Signature Motif Blocks both Archaeosortase-Dependent C-Terminal Cleavage and Prenyl Lipid Attachment for the Haloferax volcanii S-Layer Glycoprotein. J Bacteriol 198:808–15.
48. Patro M, Duggin IG, Albers SV, Ithurbide S. 2023. "Influence of plasmids, selection markers and auxotrophic mutations on Haloferax volcanii cell shape plasticity". Front Microbiol 14:1270665.
49. Wolfe AJ, Berg HC. 1989. Migration of bacteria in semisolid agar. Proc Natl Acad Sci U S A 86:6973–7.
50. Colin R, Ni B, Laganenka L, Sourjik V. 2021. Multiple functions of flagellar motility and chemotaxis in bacterial physiology. FEMS Microbiology Reviews 45.
51. Laass S, Monzon VA, Kliemt J, Hammelmann M, Pfeiffer F, Förstner KU, Soppa J. 2019. Characterization of the transcriptome of Haloferax volcanii, grown under four different conditions, with mixed RNA-Seq. PLoS One 14:e0215986.
52. Babski J, Haas KA, Näther-Schindler D, Pfeiffer F, Förstner KU, Hammelmann M, Hilker R, Becker A, Sharma CM, Marchfelder A, Soppa J. 2016. Genome-wide identification of transcriptional start sites in the haloarchaeon Haloferax volcanii based on differential RNA-Seq (dRNA-Seq). BMC Genomics 17:629.
53. Albers S-V, Jarrell KF. 2018. The Archaellum: An Update on the Unique Archaeal Motility Structure. Trends in Microbiology 26:351–362.
54. Hackley RK, Hwang S, Herb JT, Bhanap P, Lam K, Vreugdenhil A, Darnell CL, Pastor MM, Martin JH, Maupin-Furlow JA, Schmid AK. 2024. TbsP and TrmB jointly regulate gapII to influence cell development phenotypes in the archaeon Haloferax volcanii. Molecular Microbiology 121:742–766.
55. Liao Y, Vogel V, Hauber S, Bartel J, Alkhnbashi OS, Maaß S, Schwarz TS, Backofen R, Becher D, Duggin IG, Marchfelder A. 2021. CdrS Is a Global Transcriptional Regulator Influencing Cell Division in Haloferax volcanii. mBio 12:e0141621.

56. Nagel C, Machulla A, Zahn S, Soppa J. 2019. Several One-Domain Zinc Finger μ-Proteins of Haloferax Volcanii Are Important for Stress Adaptation, Biofilm Formation, and Swarming. Genes (Basel) 10.
57. McMillan LJ, Hwang S, Farah RE, Koh J, Chen S, Maupin-Furlow JA. 2018. Multiplex quantitative SILAC for analysis of archaeal proteomes: a case study of oxidative stress responses. Environ Microbiol 20:385–401.
58. Üresin D, Schulte J, Morgner N, Soppa J. 2024. C(P)XCG Proteins of Haloferax volcanii with Predicted Zinc Finger Domains: The Majority Bind Zinc, but Several Do Not. Int J Mol Sci 25.
59. Tarasov VY, Besir H, Schwaiger R, Klee K, Furtwängler K, Pfeiffer F, Oesterhelt D. 2008. A small protein from the bop-brp intergenic region of Halobacterium salinarum contains a zinc finger motif and regulates bop and crtB1 transcription. Mol Microbiol 67:772–80.
60. Tarasov V, Schwaiger R, Furtwängler K, Dyall-Smith M, Oesterhelt D. 2011. A small basic protein from the brz-brb operon is involved in regulation of bop transcription in Halobacterium salinarum. BMC Mol Biol 12:42.
61. Sharma AK, Walsh DA, Bapteste E, Rodriguez-Valera F, Ford Doolittle W, Papke RT. 2007. Evolution of rhodopsin ion pumps in haloarchaea. BMC Evolutionary Biology 7:79.
62. Deatherage DE, Barrick JE. 2014. Identification of mutations in laboratory-evolved microbes from next-generation sequencing data using breseq. Methods Mol Biol 1151:165–88.
63. Mogro EG, Ambrosis NM, Lozano MJ. 2021. Easy identification of insertion sequence mobilization events in related bacterial strains with ISCompare. G3 Genes|Genomes|Genetics 11.
64. Allers T, Ngo H-P, Mevarech M, Lloyd RG. 2004. Development of Additional Selectable Markers for the Halophilic Archaeon Haloferax volcanii Based on the leuB and trpA Genes. Applied and Environmental Microbiology 70:943–953.
65. Allers T, Barak S, Liddell S, Wardell K, Mevarech M. 2010. Improved Strains and Plasmid Vectors for Conditional Overexpression of His-Tagged Proteins in Haloferax volcanii. Applied and Environmental Microbiology 76:1759–1769.
66. Dyall-Smith M. 2008. The Halohandbook: protocols for haloarchaeal genetics. Haloarchaeal Genetics Laboratory, Melbourne 14.
67. Sambrook J, Russell DW. 2006. Preparation and Transformation of Competent E. coli Using Calcium Chloride. CSH Protoc 2006.
68. Schindelin J, Arganda-Carreras I, Frise E, Kaynig V, Longair M, Pietzsch T, Preibisch S, Rueden C, Saalfeld S, Schmid B, Tinevez J-Y, White DJ, Hartenstein V, Eliceiri K, Tomancak P, Cardona A. 2012. Fiji: an open-source platform for biological-image analysis. Nature Methods 9:676–682.
69. Stirling DR, Swain-Bowden MJ, Lucas AM, Carpenter AE, Cimini BA, Goodman A. 2021. CellProfiler 4: improvements in speed, utility and usability. BMC Bioinformatics 22:433.

70. Schindelin J, Arganda-Carreras I, Frise E, Kaynig V, Longair M, Pietzsch T, Preibisch S, Rueden C, Saalfeld S, Schmid B, Tinevez JY, White DJ, Hartenstein V, Eliceiri K, Tomancak P, Cardona A. 2012. Fiji: an open-source platform for biological-image analysis. Nat Methods 9:676–82.
71. Ershov D, Phan M-S, Pylvänäinen JW, Rigaud SU, Le Blanc L, Charles-Orszag A, Conway JRW, Laine RF, Roy NH, Bonazzi D, Duménil G, Jacquemet G, Tinevez J-Y. 2022. TrackMate 7: integrating state-of-the-art segmentation algorithms into tracking pipelines. Nature Methods 19:829–832.
72. Rados T, Andre K, Cerletti M, Bisson A. 2023. A sweet new set of inducible and constitutive promoters in Haloferax volcanii. Frontiers in Microbiology Volume 14 - 2023.
73. Li H. 2018. Minimap2: pairwise alignment for nucleotide sequences. Bioinformatics 34:3094–3100.
74. Li H, Handsaker B, Wysoker A, Fennell T, Ruan J, Homer N, Marth G, Abecasis G, Durbin R. 2009. The Sequence Alignment/Map format and SAMtools. Bioinformatics 25:2078–9.
75. Liao Y, Smyth GK, Shi W. 2019. The R package Rsubread is easier, faster, cheaper and better for alignment and quantification of RNA sequencing reads. Nucleic Acids Res 47:e47.
76. Love MI, Huber W, Anders S. 2014. Moderated estimation of fold change and dispersion for RNA-seq data with DESeq2. Genome Biology 15:550.
77. Zhu A, Ibrahim JG, Love MI. 2018. Heavy-tailed prior distributions for sequence count data: removing the noise and preserving large differences. Bioinformatics 35:2084–2092.
78. Pfaffl MW. 2001. A new mathematical model for relative quantification in real-time RT–PCR. Nucleic Acids Research 29:e45–e45.

FIGURES

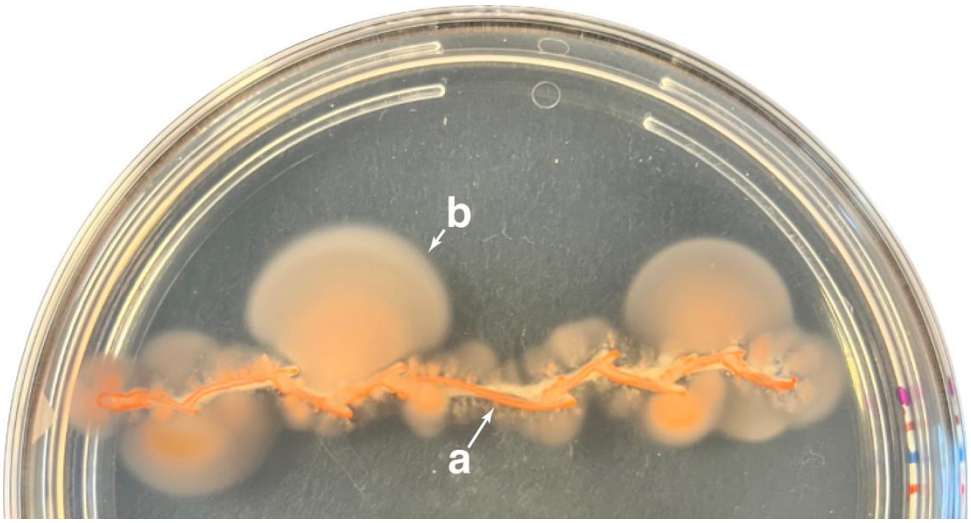

Figure 1. Isolation of Quorum sensing bypass mutants. Cultures were streaked on 25% CM soft-agar plates and incubated for 4–5 days. For better feature observation, this representative plate was stored at room temperature for one week to allow cells to darken. (a) Non-motile cells from the initial streak. (b) Motile flare containing a spontaneous QS bypass mutant

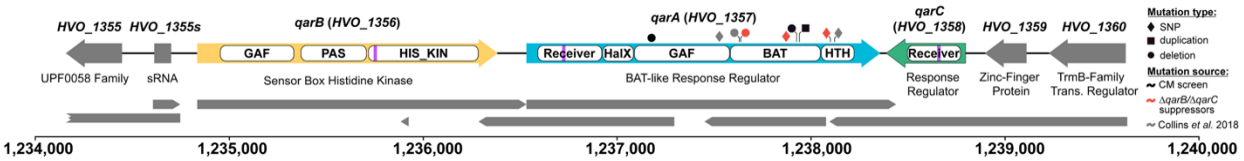

Figure 2. Genomic context, domains, and spontaneous mutations of *qarA*. Arrows representing genes surrounding *qarA* are annotated with locus tag numbers above and protein product names below. Grey arrows indicate the transcript map reported by (51); scale bar and nucleotide numbering are shown below. The types and positions of *qarA* mutations in this study and by Collins *et al*. (34) are indicated by symbols above *qarA* (key right). White boxes within gene arrows denote protein domains identified by InterProScan in the Interpro database for each gene: HVO_1356 (QarB), histidine kinase (D4GXP2); HVO_1357 (QarA), BAT-like response regulator (D4GXP4); HVO_1358 (QarC), response regulator (D4GXP7). Domains include GAF (IPR029016), PAS (IPR035965), HIS_KIN (IPR005467), Receiver (IPR001789), HalX (IPR013971), BAT (IPR031803), and HTH-10 (IPR007050). Purple lines indicate approximate position of phosphorylatable residues Asp-67 (QarA), Asp-58 (QarC), His-243 (QarB) within their Receiver or HIS_KIN domains respectively.

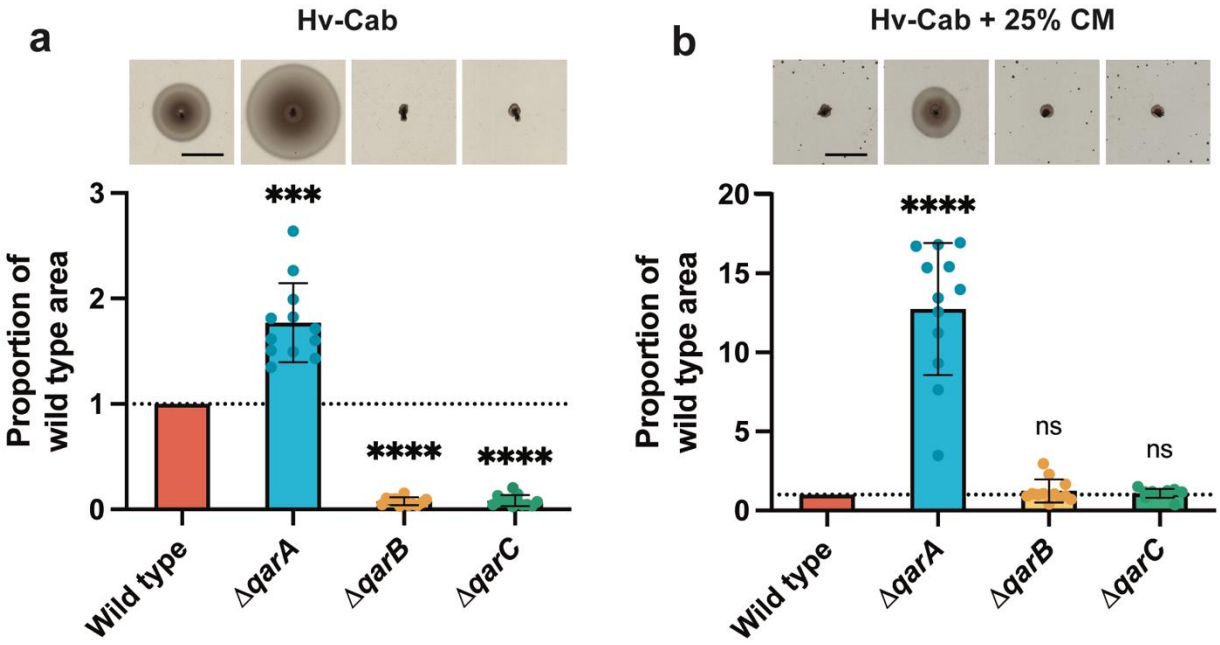

Figure 3. Deletion of *qarA* causes hypermotility while Δ*qarB* and Δ*qarC* abolish motility. Cells were stab-inoculated into 0.35% (w/vol) agar plates containing Hv-Cab medium (a) or Hv-Cab medium supplemented with 25% CM (b), incubated for 2 days at 45 °C, then stored 1-3 days at room temperature before imaging. Halo area (mm^2) was normalized to wild type. Representative halo images are shown above their corresponding quantification. Scale bar represents 1cm. Error bars indicate SD from twelve biological replicates per strain over three independent experiments; dots represent individual halos values. Statistical analysis was performed using nested one-way ANOVA on non-

normalized halo areas with multiple comparisons to wild type. ns > 0.05, *** P < 0.001, **** P < 0.0001.

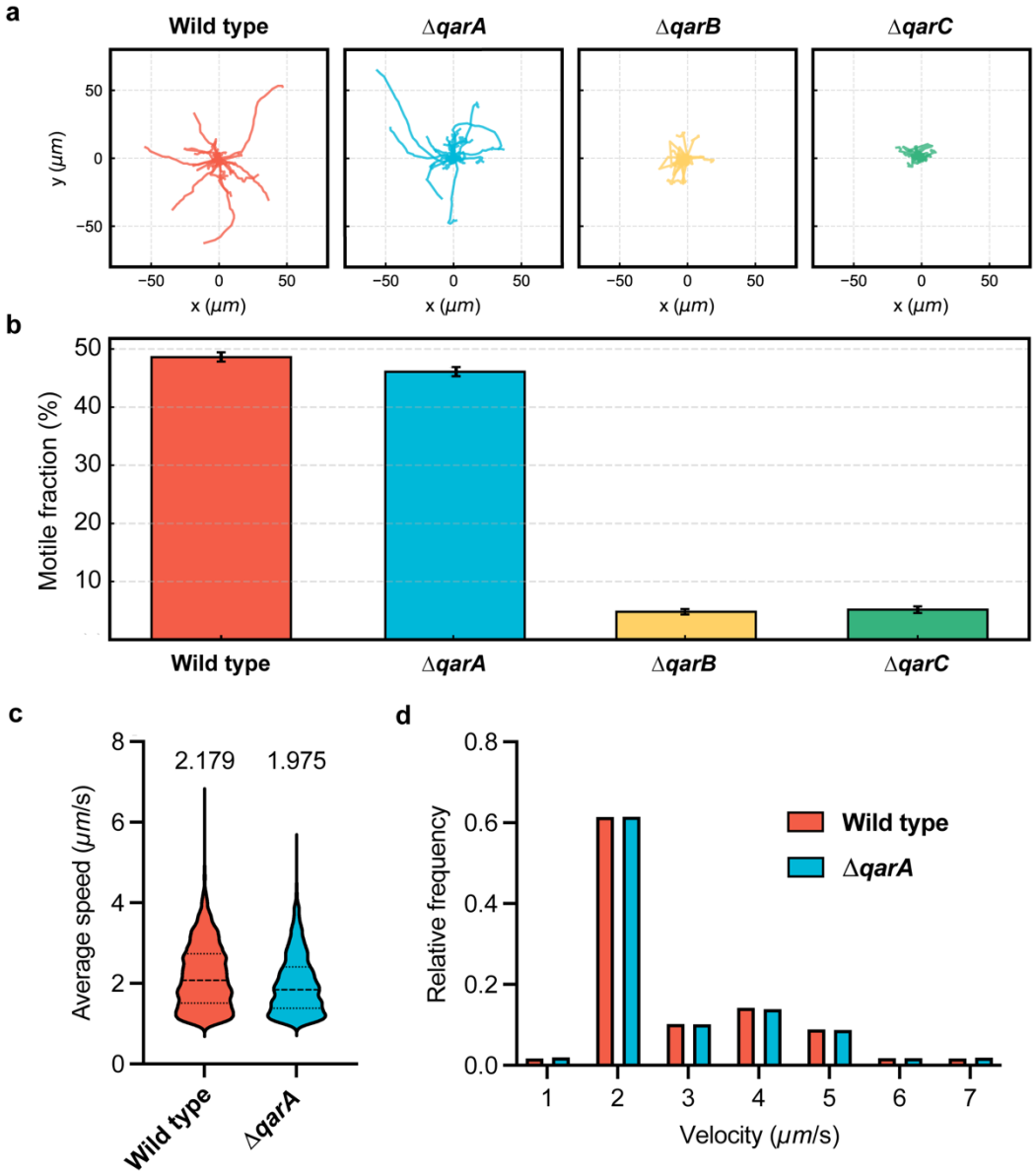

1018 **Figure 4. Δ*qarB* and Δ*qarC* are non-motile in early-log liquid culture while Δ*qarA***
1019 **cells display motility behaviors comparable to wild type.**C ells were grown to early-log
1020 phase (OD_{600} = 0.045–0.050) and diluted 1:5 (wild type, Δ*qarA*) or 1:2 (Δ*qarB*, Δ*qarC*) in
1021 pre-heated motility buffer. Diluted cultures were loaded into pre-prepared motility
1022 chambers (see Methods) and imaged immediately under brightfield illumination.
1023 Swimming behavior was recorded at 5 fps for 5 min, and trajectories were extracted in FIJI
1024 and analyzed using a custom TrackMate-based macro. This resulted in >2000 trajectories
1025 for each strain from two independent experiments. (a) Representative single-cell
1026 trajectories for each strain. (b) Fraction of motile cells (average swimming speed >1μm/s)
1027 within each population, error bars represent SD. (c) Distribution of average swimming
1028 speeds for motile strains; average speeds listed above. (d) Relative frequency of
1029 instantaneous cell velocities.
1030

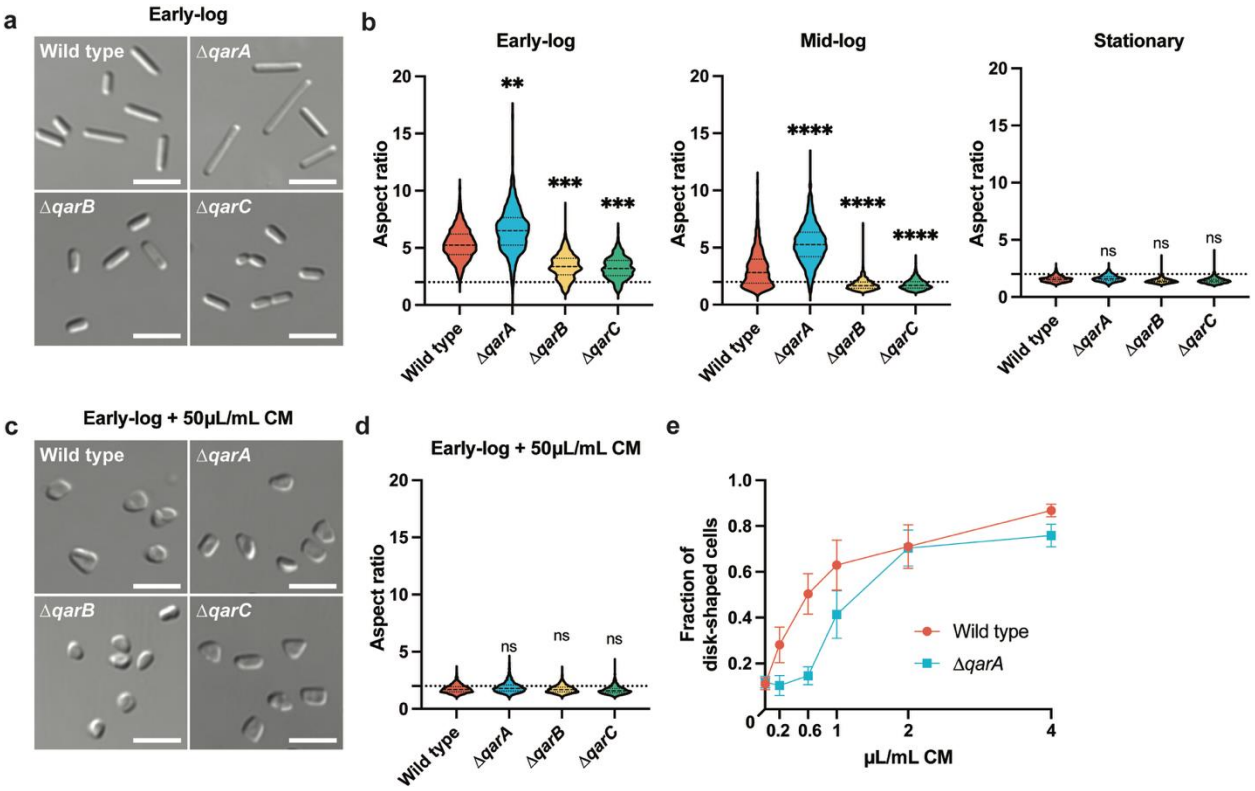

1031

1032 **Figure 5. Δ*qarA* cells show reduced sensitivity to DFS signals.** Cultures were grown to
1033 OD_{600} 0.045–0.050 (early log), 0.30 (mid log), or stationary phase (~72 h; OD_{600} 1.8–3.0).
1034 Differential interference contrast images are shown for (a) early-log cultures without
1035 additive and (c) with 1% [vol/vol] CM. Scale bar is 10μm. Cell shape quantification was
1036 performed on three biological replicates per strain in three independent experiments for
1037 each growth phase without additive (b) or at early-log with 1% [vol/vol] CM (d). Aspect
1038 ratio (major axis divided by minor axis) was calculated using CellProfiler; values < 2

1039 (dashed line) indicate disks, and values > 2 indicate rods, with larger ratios reflecting more
1040 elongated rods. Statistical analysis performed via nested one-way ANOVA with multiple
1041 comparisons to wild type. ns $P > 0.05$; ** $P < 0.01$; *** $P < 0.001$; **** $P < 0.0001$. (e) Wild-
1042 type and Δ*qarA* cultures grown to early-log with varying CM concentrations were analyzed
1043 for the resulting fraction of disk-shaped cells using CellProfiler eccentricity values (foci of
1044 ellipse-shaped object divided by major axis); values <0.9 indicate disks, and >0.9 indicate
1045 rods. Error bars represent SD of three biological replicates per strain across three
1046 independent experiments.
1047
1048
1049
1050
1051
1052

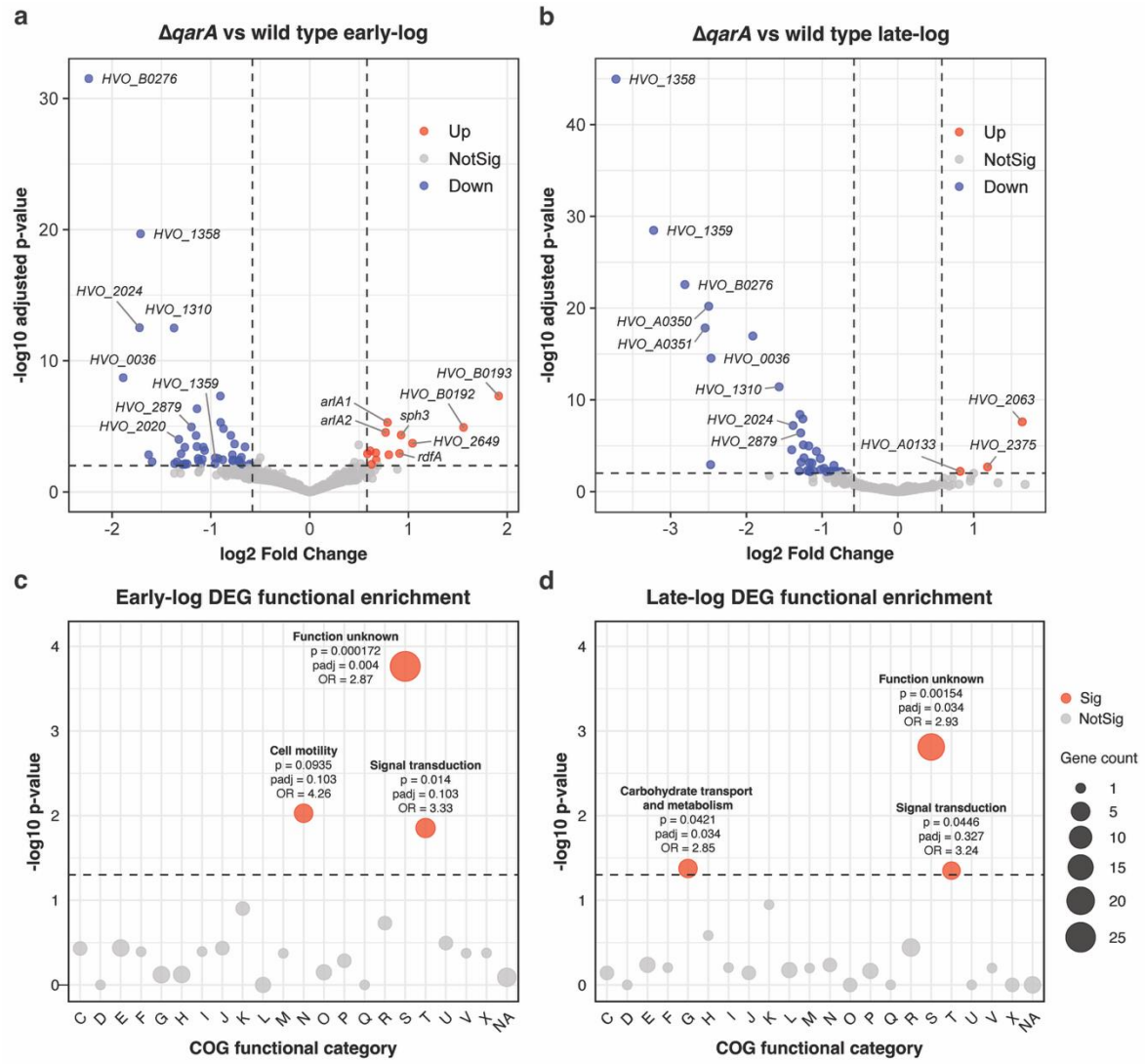

Figure 6. QarA regulates expression of motility and cell-shape determinant genes. Volcano plots depict differential gene expression in *Hfx. volcanii* between Δ*qarA* and wild-type strains during (a) early-log (motile condition) and (b) late-log (non-motile condition) growth. Each point represents a single gene, with genes of interest annotated. Genes with $|\log_2$ fold-change$|$ > 0.58 and adjusted p-value (Benjamini–Hochberg) < 0.01 were considered significantly differentially expressed. *qarA* was excluded from plots to better visualize other DEGs. Bubble plots show significantly enriched COG functional categories among DEGs identified in the Δ*qarA* vs. wild type comparison during early-log (c) and late-log (d) growth. The size of each bubble corresponds to the number of DEGs in the category, and bubble color indicates enrichment significance which was determined by Fisher's exact test. Categories were considered enriched if they had an unadjusted p-value < 0.05. For significantly enriched categories, the COG function, p-value, adjusted p-value (Benjamini–Hochberg), and odds ratio are reported.

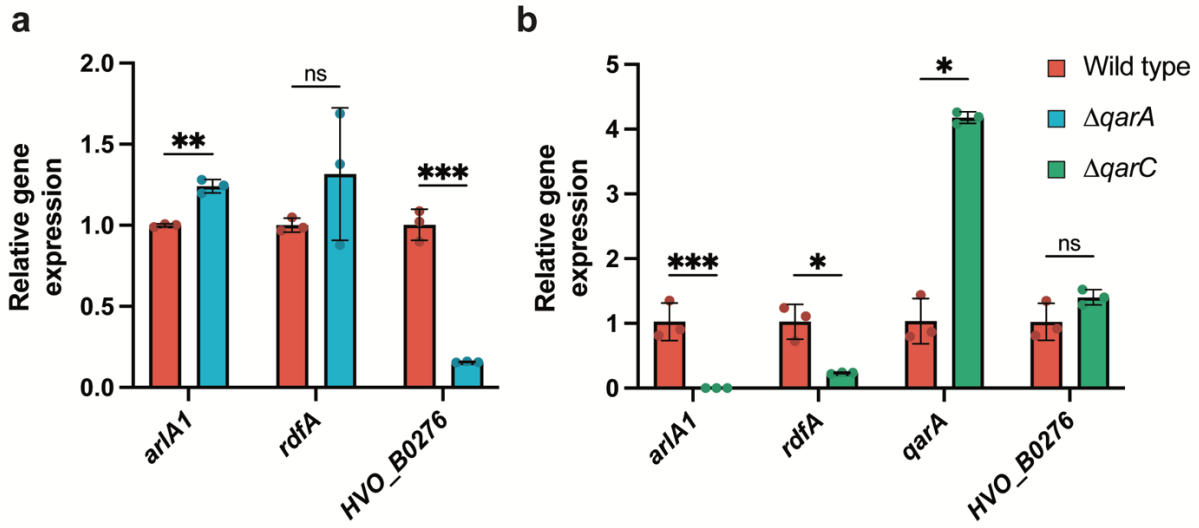

Figure 7. qRT-PCR analysis of Δ*qarA* confirms differential regulation of DEGs identified by RNA-seq while Δ*qarC* displays reciprocal regulation of key DEGs. Reactions were performed using primers for *eif1a*, *arlA1*, *rdfA*, *qarA*, and *HVO_B0276* under the following conditions: (a) wild type vs. Δ*qarA*, and (b) wild type vs. Δ*qarC*. Relative expression levels were calculated using the Pfaffl method, normalized to eif1a, and expressed relative to wild-type controls. Error bars indicate SD of three biological replicates, each with three technical replicates. Statistical significance was determined by $\log_2$-transforming relative expression values and performing unpaired t-tests with Welch's correction. ns $P > 0.05$, * $P < 0.05$, ** $P < 0.01$ *** $P < 0.001$.

1094

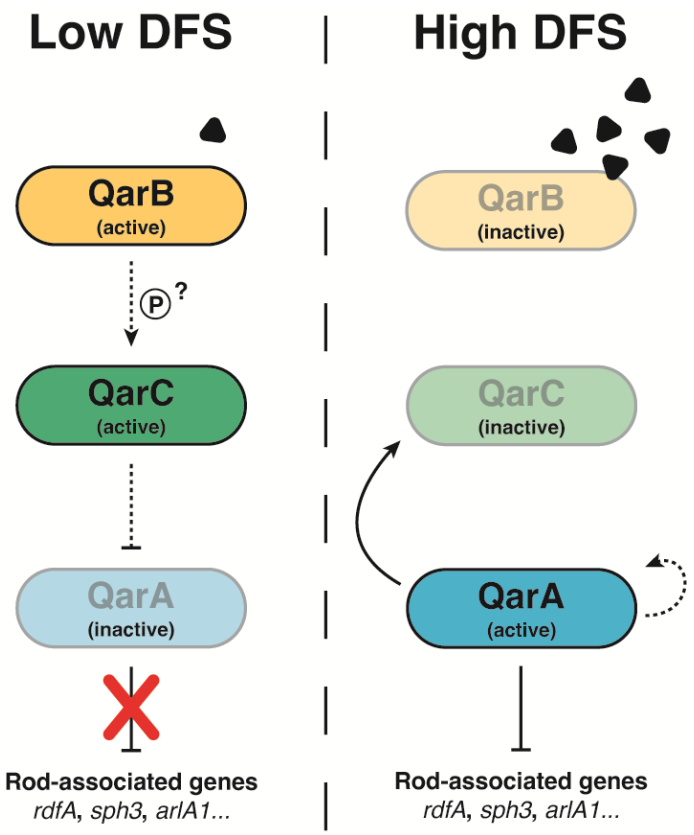

1095 **Figure 8. Proposed model of the DFS-responsive QarABC regulatory system.** RNA-seq
1096 and qRT-PCR data reveal QarA regulatory targets (solid lines), while other phenotypic,
1097 genetic, and transcriptomic observations support putative interactions (dashed lines).
1098
1099
1100
1101
1102
1103
1104
1105
1106
1107
1108
1109
1110
1111
1112

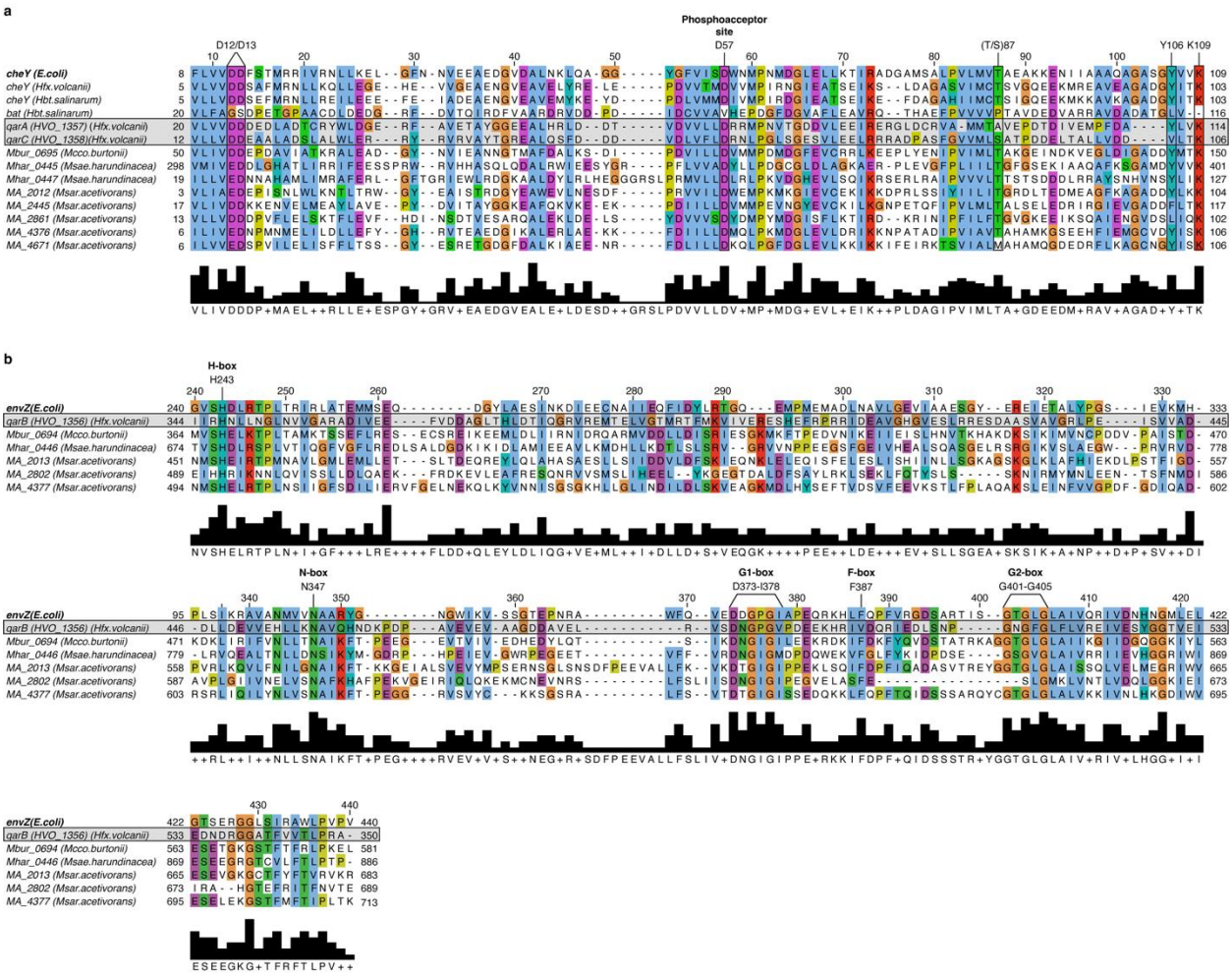

Figure S1. Multiple sequence alignment of *Hfx. volcanii* histidine kinase and response regulator proteins (QarABC) with representative archaeal and Escherichia coli sequences. Alignments were visualized in Jalview, with shading based on the default ClustalX coloring scheme. A conservation histogram and consensus sequence are shown below each alignment. In panel (a), key catalytic residues of *E. coli* CheY (D12–D13, D57, T/S87, Y106, K109; UniProt: P0AE67) are indicated above the alignment, with residue numbering referenced to CheY. In panel (b), conserved motifs of *E. coli* EnvZ (H-box, N, G1, F, and G2 boxes; UniProt: P0AEJ4) are highlighted above the alignment, with residue numbering referenced to EnvZ. CheY D57 corresponds to D67 in QarA and D58 in QarC, and EnvZ H243 corresponds to H347 in QarB.

1129

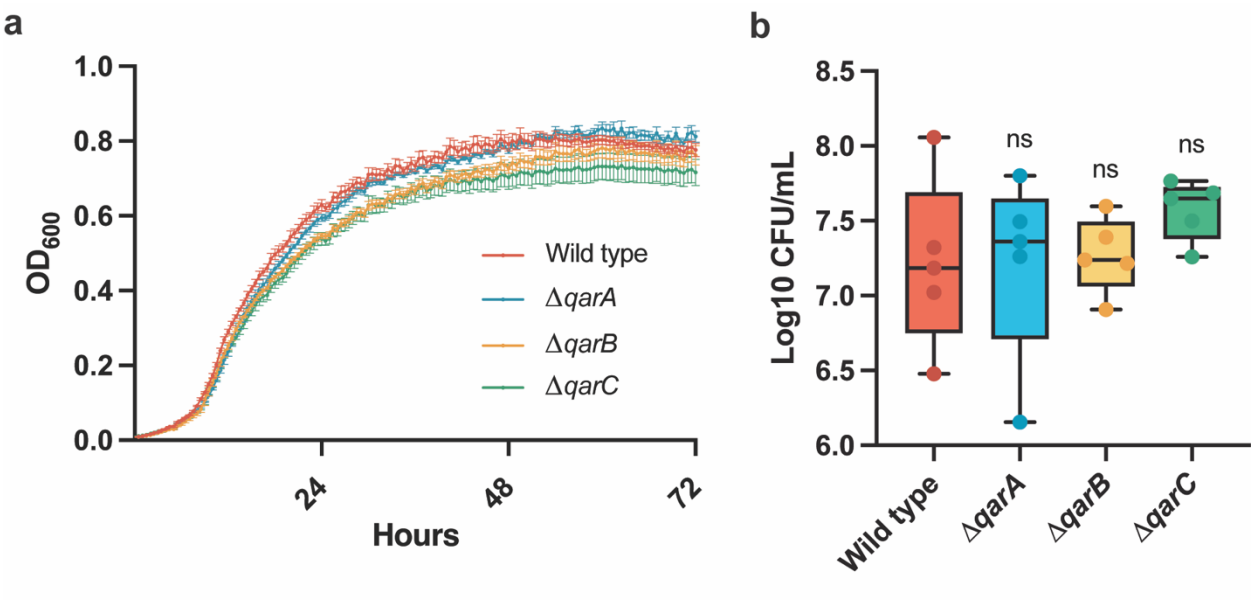

1130 **Figure S2. Growth and viability of QarABC mutants.** (a) Growth curves of wild-type and
1131 QarABC mutants cultured in liquid medium at 45 °C for 72h. Data represent the mean and
1132 SD of four biological replicates. (b) Viable cell counts ($\log_{10}$ CFU/mL) of mid-log-phase
1133 cultures determined by serial dilution and plating on Hv-Cab agar. Error bars represent SD
1134 of five biological replicates from five independent experiments.
1135
1136
1137
1138
1139
1140
1141
1142
1143
1144
1145
1146
1147
1148
1149
1150
1151
1152

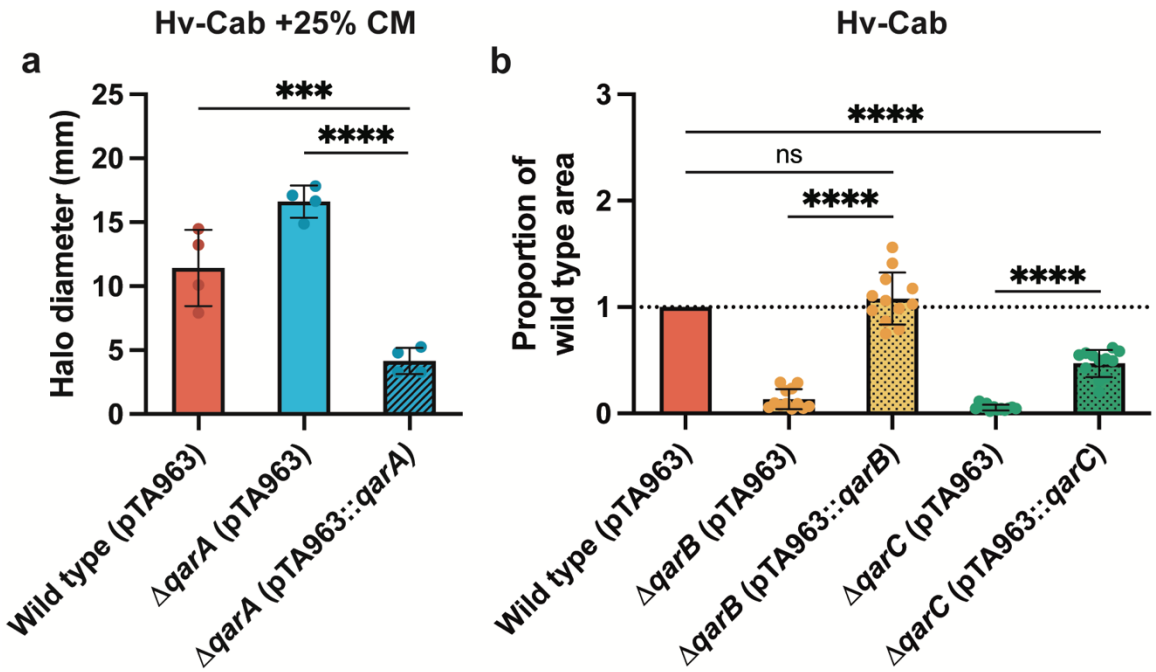

Fig. S3. ***qarA* overexpression represses motility; *qarABC* are complementable *in trans*.** Cells were stab-inoculated into 0.35% (w/v) agar plates containing (a) Hv-Cab medium with 25% CM or (b) Hv-Cab medium alone, incubated for 2 days at 45 °C, and stored for 1–3 days at room temperature before imaging. Motility was quantified by (a) halo diameter (mm) or (b) halo area (mm^2) normalized to the wild type. Error bars indicate SD from (a) four biological replicates per strain or (b) twelve biological replicates across three independent experiments; dots represent individual halo values. Statistical analysis was performed using nested one-way ANOVA comparing complementation strains to their respective knockouts and to wild type. Non-normalized halo areas were used for analysis in (b). ns > 0.05, *** P < 0.001, **** P < 0.0001.

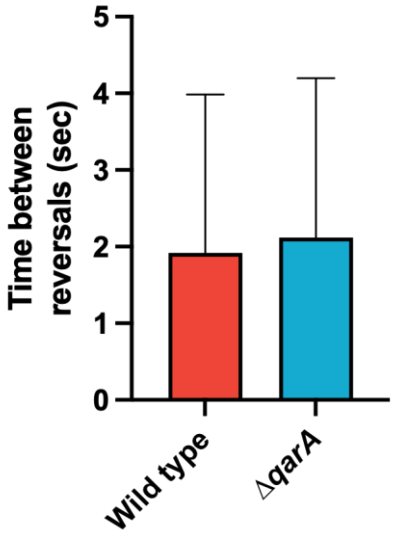

Fig. S4. Δ*qarA* appears to have a similar reversal frequency to wild type. Cells were grown to early-log phase (OD_{600} = 0.045–0.050) and diluted 1:5. Diluted cultures were loaded into pre-prepared motility chambers (see Methods) and imaged immediately under brightfield illumination. Swimming behavior was recorded at 5 fps for 5 min, and trajectories were extracted in FIJI and analyzed using a custom TrackMate-based macro. This resulted in >2000 trajectories for each strain from two independent experiments. Reversal frequency was determined by the average time between two subsequent >90° turns for each tracked cell over its entire track. Error bars represent SEM.

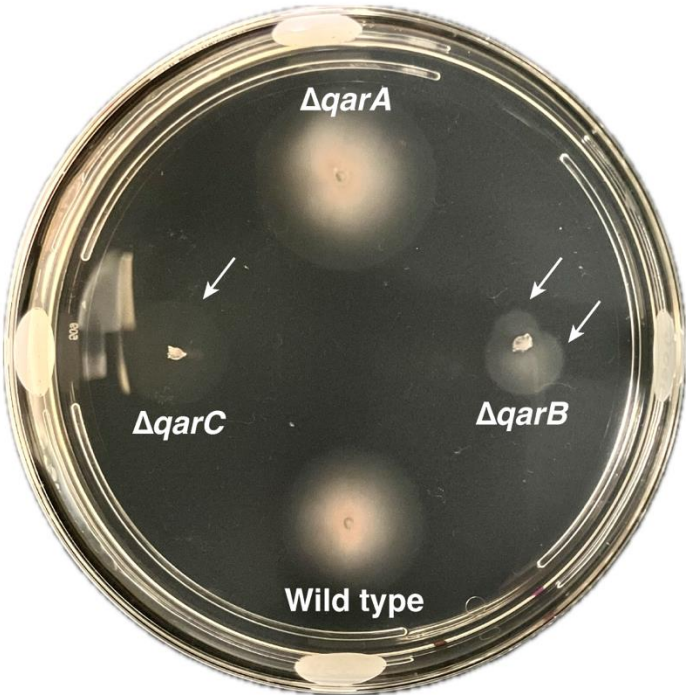

Fig. S5. Representative soft-agar plate displaying motile suppressors of Δ*qarB* and Δ*qarC.* Cells were stab-inoculated into 0.35% (w/vol) agar plates containing Hv-Cab medium and incubated for 2 days at 45 °C, then stored 1-3 days at room temperature before imaging. White arrows represent spontaneous suppressor mutants from non-motile strains.

1221
1222
1223 **TABLES**
1224
1225 **Table 1. Genome alterations in *Hfx. volcanii* mutants less responsive to DFS-mediated**
1226 **motility inhibition.**
1227

Isolate[§]	Affected Gene(s)[†]	Mutation	Position on gene	Secondary Mutation(s)[‡]	Gene Product
MG32	*HVO_1212* (*cirA*)	P168L	505/741 nt	Yes	KaiC-type circadian clock protein CirA
SB1	*HVO_1212* (*cirA*)	Δ1 bp	657/741 nt		KaiC-type circadian clock protein CirA
SB7	*HVO_1212* (*cirA*)	+1 bp	657/741 nt		KaiC-type circadian clock protein CirA
SB13	*HVO_1212* (*cirA*)	F133S	399/741 nt		KaiC-type circadian clock protein CirA
SB15	*HVO_1212* (*cirA*)	Y43D	128/741 nt		KaiC-type circadian clock protein CirA
MG6	*HVO_1357 (qarA)*	L529P	1586/1749 nt		Receiver/bat box HTH-10 family transcription regulator
SB17	*HVO_1357 (qarA)*	Δ261 bp	1412-1672/1749 nt		Receiver/bat box HTH-10 family transcription regulator
SB18	*HVO_1357 (qarA)*	+46bp	1,424/1,749 nt		Receiver/bat box HTH-10 family transcription regulator
SB19	*HVO_1357 (qarA)*	+46bp	1,424/1,749 nt		Receiver/bat box HTH-10 family transcription regulator
MG4	*HVO_2248*	Δ4 bp	803-806/816 nt	Yes	Uncharacterized protein
MG7	*HVO_2239–HVO_2298*	Δ67,424 bp			66 Genes including HVO_2248 (Uncharacterized protein)
SB2	*HVO_A0350**	K199N	597/642 nt	Yes	Uncharacterized protein
SB20	*HVO_A0350**	K199N	597/642 nt		Uncharacterized protein
MG5	*HVO_1136* (*pgsA1*)*	Δ9 bp	409-417/825 nt	Yes	CDP-alcohol 1-archaetidyltransferase
MG8	*HVO_2176* (*ddfA*)	+138bp	142/201 nt		Disk-determining factor A
MG10	*HVO_2001–HVO_2069*	Δ69,438 bp			72 genes
MG15	*HVO_2885* (*gltP2*)*	A352T	1,056/1,305 nt		SDF family transport protein (probable substrate glutamate/asparta
MG27	*HVO_2830* (*cdc48a*)	D339G	1,016/2,232 nt		AAA-type ATPase (CDC48 subfamily)
SB3	*HVO_2649*	T→A	-35 nt upstream		Uncharacterized protein

1228
1229 [§]Isolate names starting with MG indicate those from the first screen while SB indicates
1230 those from the second (see methods). [†]Mutations predicted by BreSeq (62) and not found
1231 in Pohlschröder lab H53 strain, sorted by frequency. *Manual assertion using marginal
1232 evidence for isolates where BreSeq did not predict a mutation. [‡]BreSeq-predicted
1233 mutations in addition to primary affected gene. Full details for each isolate are provided in
1234 Table S1. The BreSeq report for the Pohlschröder lab H53 strain background can be found
1235 at https://doi.org/10.5281/zenodo.17419175.